Lactate supply overtakes glucose when neural
computational and cognitive loads scale up

Yulia Dembitskaya, Charlotte Piette, Sylvie Perez, Hugues Berry, Pierre J
Magistretti, Laurent Venance

▶ To cite this version:

Yulia Dembitskaya, Charlotte Piette, Sylvie Perez, Hugues Berry, Pierre J Magistretti, et al..
Lactate supply overtakes glucose when neural computational and cognitive loads scale up. Proceedings of the National Academy of Sciences of the United States of America, 2022, 119 (47),
10.1073/pnas.2212004119 . hal-03922367

HAL Id: hal-03922367
https://hal.inria.fr/hal-03922367

Submitted on 4 Jan 2023

HAL is a multi-disciplinary open access
archive for the deposit and dissemination of sci-
entific research documents, whether they are pub-
lished or not. The documents may come from
teaching and research institutions in France or
abroad, or from public or private research centers.

L'archive ouverte pluridisciplinaire HAL, est
destinée au dépôt et à la diffusion de documents
scientifiques de niveau recherche, publiés ou non,
émanant des établissements d'enseignement et de
recherche français ou étrangers, des laboratoires
publics ou privés.

Lactate supply overtakes glucose when neural computational and cognitive loads scale up

Yulia Dembitskaya[a], Charlotte Piette[a], Sylvie Perez[a], Hugues Berry[b,c,1,2] 🆔, Pierre J. Magistretti[d,e,1,2], and Laurent Venance[a,1,2] 🆔

Neural computational power is determined by neuroenergetics, but how and which energy substrates are allocated to various forms of memory engram is unclear. To solve this question, we asked whether neuronal fueling by glucose or lactate scales differently upon increasing neural computation and cognitive loads. Here, using electrophysiology, two-photon imaging, cognitive tasks, and mathematical modeling, we show that both glucose and lactate are involved in engram formation, with lactate supporting long-term synaptic plasticity evoked by high-stimulation load activity patterns and high attentional load in cognitive tasks and glucose being sufficient for less demanding neural computation and learning tasks. Indeed, we show that lactate is mandatory for demanding neural computation, such as theta-burst stimulation, while glucose is sufficient for lighter forms of activity-dependent long-term potentiation (LTP), such as spike timing–dependent plasticity (STDP). We find that subtle variations of spike number or frequency in STDP are sufficient to shift the on-demand fueling from glucose to lactate. Finally, we demonstrate that lactate is necessary for a cognitive task requiring high attentional load, such as the object-in-place task, and for the corresponding in vivo hippocampal LTP expression but is not needed for a less demanding task, such as a simple novel object recognition. Overall, these results demonstrate that glucose and lactate metabolism are differentially engaged in neuronal fueling depending on the complexity of the activity-dependent plasticity and behavior.

neuroenergetic | synaptic plasticity | learning and memory | lactate | glucose

Brain activity and performance are tightly constrained by neurovasculature–neuroenergetic coupling (1–3). Neuroenergetics, that is, brain energy metabolism, relies on the blood supply of glucose from the circulation. Evidence accrued over the last two decades has indicated that blood glucose is taken up during synaptic activity (4, 5), mainly by glial cells (astrocytes and oligodendrocytes), and metabolized by aerobic glycolysis, resulting in the release of lactate before transport to neurons as an energy substrate (6–13) necessary for optimized neuronal coding and memory consolidation (14–22). When astrocytes constitute the source of lactate, this process is known as the astrocyte–neuron lactate shuttle in which lactate is transferred from astrocytes to neurons through monocarboxylate transporters, providing an energy substrate for neurons (7). Indeed, lactate can be rapidly metabolized to pyruvate, enter the tricarboxylic acid cycle, and feed the mitochondrial respiratory chain to produce ATP. Other fates of glucose include its glial storage in the form glycogen (7, 23, 24); some degree of glucose uptake occurs in neurons via transporters mainly aimed at feeding the pentose phosphate shunt to produce reducing equivalents (25–27), which is involved in olfactory memory in *Drosophila* (28). Nevertheless, the nature of the energy substrate, glucose versus lactate, allocated to various forms of memory engram and cognitive load is not known.

Here, we tested various forms of activity patterns (rate- and time-coding) for Hebbian long-term synaptic plasticity expression in rat cornu ammonis 1 (CA1) hippocampal pyramidal cells and behavioral tasks with increasing cognitive loads to determine under which conditions glucose and/or lactate are crucial for engram formation and memory. To this end, using brain slice and in vivo electrophysiology, two-photon imaging, mathematical modeling, and recognition memory tasks, we show that astrocytic lactate is mandatory for demanding neural computation, while glucose is sufficient for lighter forms of activity-dependent long-term potentiation (LTP) and that subtle variations of action potential amount or frequency are sufficient to direct the energetic dependency from glucose to lactate. Furthermore, we demonstrate that lactate is necessary for a cognitive task requiring high attentional load (object-in-place [OiP] task) and for the corresponding in vivo hippocampal potentiation but is not needed for a less demanding task (novel object recognition [NOR]). Our results demonstrate that glucose and lactate metabolism are differentially engaged in neuronal fueling depending on the

Significance

Brain activity and performance are constrained by energy metabolism. Glucose and lactate have been proposed as energy substrates for neurons allocated to various forms of memory. We demonstrate that glucose and lactate metabolism are differentially engaged in neuronal fueling depending on the activity-dependent plasticity and behavioral complexity. These results reconcile a decades-long debate regarding the nature of the neuroenergetic sources used by synaptic activity with the potential of inspiring future lines of research regarding neuroenergetic rules. The brain has high energy demands, and alterations in neuroenergetics are hallmarks of several neuropathologies. A better knowledge of the cellular and molecular mechanisms of neuroenergetics, as reported here, may be instructive in targeting energy metabolism deficits as a therapeutic approach for neurodegenerative diseases.

[1]H.B., P.J.M., and L.V. contributed equally to this work.

[2]To whom correspondence may be addressed. Email: hugues.berry@inria.fr, pierre.magistretti@kaust.edu.sa, or laurent.venance@college-de-france.fr.

complexity of the activity-dependent plasticity and behavior. Beyond reconciling a decades-long debate (7, 11, 26, 27), our results demonstrate the importance of distinguishing specific cellular and molecular mechanisms because the corresponding cognitive perturbations might depend on whether lactate or glucose metabolism is perturbed.

Results

Rate and Time Coding Rely Differently on Lactate Availability to Neurons. To investigate the relative involvement of glucose and lactate metabolism in synaptic plasticity, we tested two activity-dependent forms of LTP at hippocampal CA1 pyramidal cells (Fig. 1 A–C), aiming to reflect two levels of neural computation. We chose two distinct Hebbian activity patterns: 1) a rate-coding paradigm involving a high stimulation load (200 stimulations; 5× theta-burst stimulation [5-TBS] with nested high-frequency [100 Hz] stimulations within slower frequencies [5 Hz] repeated five times [at 0.1 Hz]) and 2) a time-coding paradigm involving a lower stimulation load (50 stimulations; spike timing–dependent plasticity (STDP) with 50 pre- and postsynaptic paired stimulations at a low frequency [0.5 Hz]) (Fig. 1 and *SI Appendix*, Table S1). Whole-cell recordings of CA1 pyramidal cells were performed at a physiological glucose concentration (5 mM) (29) to avoid saturated nonphysiological concentrations of glucose (~15 to 25 mM) classically used in brain slice studies. In the following experiments, drugs were applied intracellularly (i-drug) via patch-clamp pipette, ensuring specific effects in the sole recorded neuron except in few cases where drugs were bath applied (e-drug). The 5-TBS and STDP paradigms induced LTP, and both were *N*-methyl-D-aspartic acid receptor (NMDAR) mediated because they were prevented by the
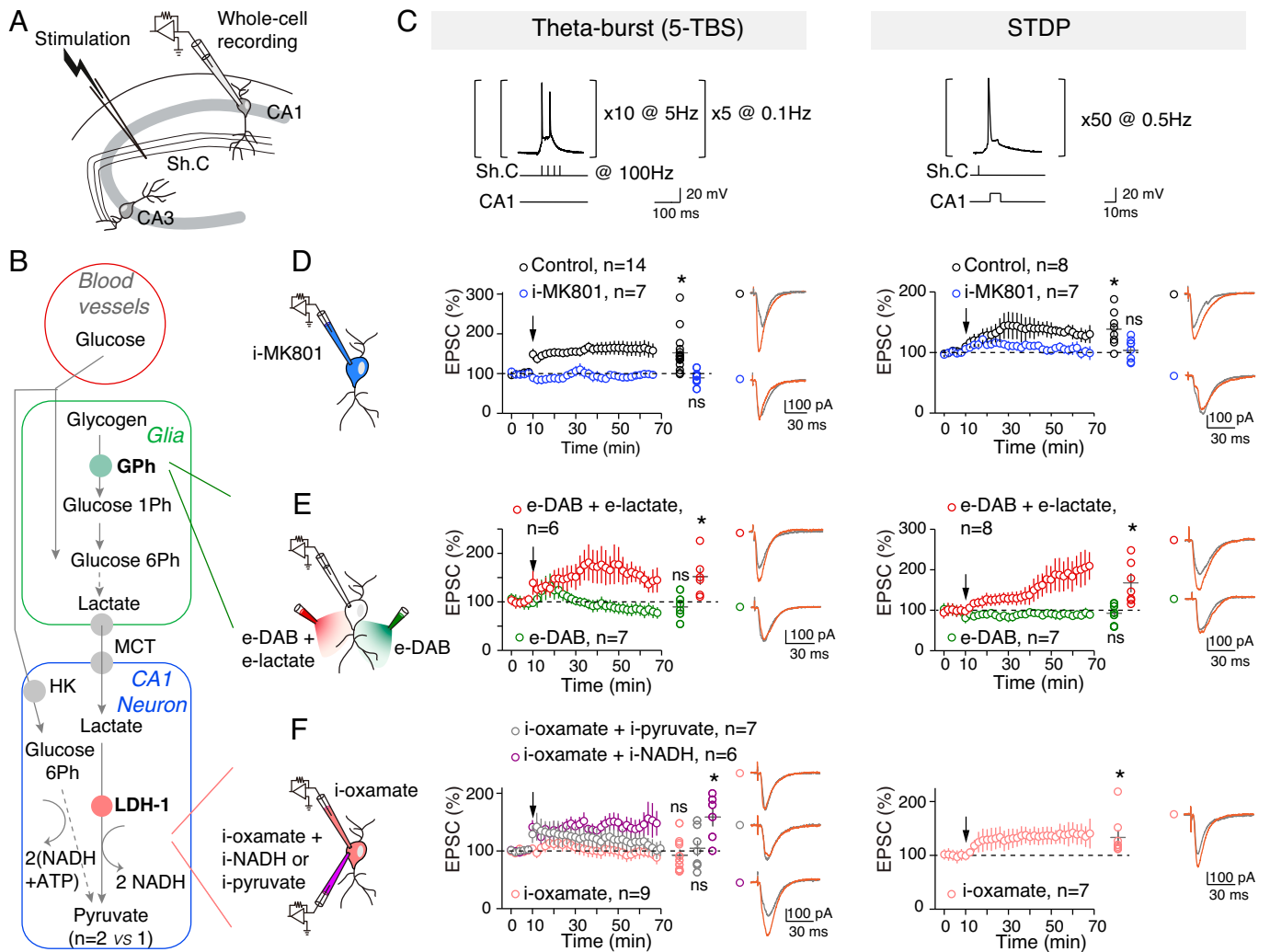

Fig. 1. 5-TBS–LTP and STDP-LTP rely differently on neuronal lactate. (*A*) Experimental setup. Sh. C, Schaffer collaterals. (*B*) Key steps of glucose transport and glia–neuron lactate transport: glycogen catalysis into glucose-1-phosphate via glycogen phosphorylase, lactate entry in neurons via monocarboxylate transporters (MCTs), and lactate conversion to pyruvate by LDH; Ph, phosphate. (*C*) 5-TBS (with nested high-frequency, 100-Hz stimulations within slower-frequency, 5-Hz stimulations repeated five times at 0.1 Hz) and STDP (50 paired pre/post stimulations at 0.5 Hz) paradigms. (*D–G*) Averaged time-course of the synaptic weight with EPSC amplitude 50–60 min after TBS or STDP paradigm. (*D*) 5-TBS–LTP and STDP-LTP (5-TBS–LTP: $P = 0056$, $n = 14$; STDP-LTP: $P = 0.0070$, $n = 8$) were NMDAR mediated (with intracellular application of i-MK801: 5-TBS, $P = 0.1562$, $n = 7$; STDP, $P = 0.6484$, $n = 7$). (*E*) Inhibition of glycogen phosphorylase with bath-applied DAB (e-DAB) prevented 5-TBS–LTP and STDP-LTP (with e-DAB: 5-TBS, $P = 0.3691$, $n = 6$; STDP, $P = 0.4213$, $n = 7$). Coapplication of DAB and lactate allowed 5-TBS–LTP and STDP-LTP ($P = 0.0311$, $n = 6$ and $P = 0.0383$, $n = 7$, respectively). LTP rescued with e-lactate was not significantly different from control (5-TBS-LTP: $P = 0.6735$; STDP-LTP: $P = 0.4155$). (*F*) Intracellular inhibition of LDH revealed distinct effects on 5-TBS and STDP expression because i-oxamate prevented 5-TBS–LTP ($P = 0.4600$, $n = 9$) but not STDP-LTP ($P = 0.0398$, $n = 7$). 5-TBS–LTP was rescued with coapplication of i-oxamate and i-NADH ($P = 0.0145$, $n = 6$ versus 5-TBS–LTP control: $P = 0.7995$) but not i-pyruvate ($P = 0.7548$, $n = 7$). Representative traces show 15 EPSCs averaged during baseline (gray) and 45 min (red) after protocols (arrows). All data are shown as mean ± SEM; *, $P < 0.05$; ns, not significant by two tailed *t* test. See *SI Appendix, Table S1*, for detailed data and statistics.

2 of 9 https://doi.org/10.1073/pnas.2212004119

pnas.org

Downloaded from https://www.pnas.org by 86.202.64.175 on November 14, 2022 from IP address 86.202.64.175.

intracellular application of the NMDAR blocker MK801 (i-MK801; 1 mM) (Fig. 1D and *SI Appendix,* Fig. S1). Because both LTP forms share the same signaling pathway, we could interpret their respective glucose/lactate dependency based on the activity patterns. We evaluated whether 5-TBS–LTP and STDP-LTP expression equally relies on lactate metabolism by sequentially inhibiting two key steps: glycogen mobilization into glucose-1-phosphate, the first step of glycogenolysis leading ultimately to glia-derived lactate, via glycogen phosphorylase and conversion of lactate into pyruvate via the neuronal lactate dehydrogenase (LDH-1) (Fig. 1B). When glial glycogenolysis was prevented by inhibiting glycogen phosphorylase with 1,4-dideoxy-1,4-imino-D-arabinitol (e-DAB; 10 μM), 5-TBS or STDP pairings failed to induce synaptic plasticity (Fig. 1E). We tested whether lactate overcomes DAB effects. With e-DAB and e-lactate (10 mM), we observed 5-TBS–LTP and STDP-LTP (Fig. 1E); LTP rescued with e-lactate was not significantly different from controls. This indicates that lactate formed from glycogenolysis is a key factor for hippocampal LTP induction (14, 16, 20). We next prevented the conversion of lactate into pyruvate by applying oxamate (an inhibitor of LDH) intracellularly (i-oxamate; 6 mM) only in the recorded neuron. Under this condition, 5-TBS did not evoke plasticity, whereas STDP-LTP could still be observed (Fig. 1F). Conversion of lactate into pyruvate was thus required for 5-TBS–LTP but not for STDP-LTP. We then tested which products of lactate conversion by LDH-1, that is, pyruvate or NADH, was needed for 5-TBS–LTP. When i-pyruvate (10 mM) was coapplied intracellularly with i-oxamate, 5-TBS did not induce plasticity, whereas 5-TBS–LTP was rescued with i-NADH (4 mM) (Fig. 1F).

As revealed by LDH inhibition, neuronal lactate appears as a key element for 5-TBS–LTP (via its metabolism to pyruvate leading to NADH production), but is not necessary for inducing a lighter form of activity-dependent plasticity involving 50 STDP pairings, which relies on glucose metabolism when lactate conversion is blocked.

Confronting Mathematical Model and Experimental Data Delineates the Energetic Needs of Synaptic Plasticity. To provide hypotheses for the differential effects of the neuronal glucose and lactate metabolism on activity-dependent plasticity, we developed a mathematical model of CA1 synaptic plasticity combined with metabolism. Our model describes the kinetics of signaling and metabolic reactions occurring in a neuro–glia unit in response to activity patterns (Fig. 2A). The postsynaptic weight is modeled as a bistable system gated by calcium and ATP; postsynaptic calcium triggers LTP when it overcomes a threshold (LTP_{Start}), while the postsynaptic ATP level triggers depotentiation when falling below a second threshold (ATP_{Thr}). Calcium influx in the postsynaptic neuron changes in response to presynaptic and postsynaptic spikes via the activation of NMDAR and voltage-gated calcium channels. ATP levels in each compartment are computed by a model of metabolic interactions with the astrocyte–neuron lactate shuttle (30) that includes, among others, glycolysis and LDH activity in glia and the postsynapse as well as glucose and lactate transfer from glia to neurons via the extracellular medium (*SI Appendix, Supplementary Materials and Methods and Supplementary Information for the Mathematical Model*). Importantly, the values of the model parameters were estimated using a subset of our experimental data taken from Figs. 1 D–G and 2B and Tables S1–S3, while model validation was performed using model predictions, that is, by checking the accuracy of the model output under experimental conditions that were not used for parameter estimation (the pharmacological

experiments of Figs. 2 D–G and 3). The model captures the amplitude and kinetics of change of the synaptic weight after 5-TBS and STDP pairings (Fig. 2B). In the model, both 5-TBS and STDP paradigms are strong enough to generate large calcium transients in the postsynaptic neuron (*SI Appendix,* Fig. S2A) that overcome the LTP_{Start} threshold, thus triggering LTP. The amplitudes of Na^+ transients in the postsynaptic neuron are much larger with 5-TBS than with STDP so that ATP consumption by Na,K^+-ATPases is larger with 5-TBS (Fig. 2C). With the model, the concept that different levels of activity pattern loads are engaged in STDP (50 pairings at 0.5 Hz) versus 5-TBS was supported by estimating the neuronal sodium and calcium influxes (that were <1 versus >3 mM and ~0.75 versus ~1.5 μM, respectively) or the amplitude of ATP consumption used for sodium extrusion (~90 versus ~300 μM; Fig. 2C and *SI Appendix,* Fig. S2A). The availability of lactate as a source of ATP keeps ATP levels well above ATP_{Thr} even after 5-TBS. LDH inhibition switches the neuron to a glycolytic regimen, an oxidized redox state where ATP level drops to 2.1 mM at rest (*SI Appendix,* Fig. S3). After STDP and with LDH inhibition, the ATP levels keep well above ATP_{Thr}, while with 5-TBS, ATP quickly fails below ATP_{Thr}, and the resulting depotentiation forbids LTP expression (Fig. 2C). Experimentally, we found that pyramidal cells recorded with lower i-ATP and i-phosphocreatine (2 and 5 mM, respectively) did not exhibit plasticity following STDP (50 pairings at 0.5 Hz) in control or i-oxamate (*SI Appendix,* Fig. S4).

Using a model-guided approach, we investigated the impact of glucose on LTP expression. Fig. 2D shows model output for TBS with LDH inhibited depending on extracellular glucose concentration. The model predicts that LTP recovers if bath glucose concentration is large enough. Experiments confirmed that with high glucose concentration (25 mM), 5-TBS–LTP was no longer sensitive to i-oxamate (Fig. 2D). Another model prediction is that the hexokinase inhibition, the first enzyme of glycolysis catalyzing the phosphorylation of glucose to glucose-6-phosphate (Fig. 1B), should not affect 5-TBS–LTP (Fig. 2E). Indeed, experimentally, a specific inhibitor of the hexokinase, mannoheptulose, applied intracellularly (i-mannoheptulose; 10 μM) did not prevent 5-TBS–LTP (Fig. 2E), confirming that 5-TBS–LTP relies on lactate and not on glucose metabolism. We next explored the glucose dependency of STDP, and, as predicted by the model, we found that i-mannoheptulose did not prevent STDP-LTP (Fig. 2F), indicating that in the absence of neuronal glycolysis, the lactate pathway is used for the expression of STDP-LTP (50 pairings at 0.5 Hz). We next doubled the number and frequency of STDP pairings (up to 100 pairings at 1 Hz) to test whether this property could be extended to other STDP forms. In confirmation of the model prediction, we found that 100 pairings at 1 Hz induced LTP with i-mannoheptulose (Fig. 2G). Interestingly, when both neuronal glucose and lactate sources were impaired by the intracellular coapplication of i-mannoheptulose and i-oxamate, (100 pairings at 1 Hz) STDP-LTP was not observed (Fig. 2G), showing that STDP relies on either glycolysis or lactate pathway. Together, these model-guided experiments show that TBS-LTP relies on lactate, although high glucose can bypass lactate fueling, whereas STDP can use either the glycolysis or lactate pathways.

Dependence on Glucose versus Lactate for LTP Expression Is Activity Pattern Linked. We varied the TBS and STDP activity patterns to delineate the sensitivity of the plasticity dependency on glucose and lactate metabolism. Model calibration relied exclusively on 5-TBS and STDP with 50 pairings at 0.5 Hz
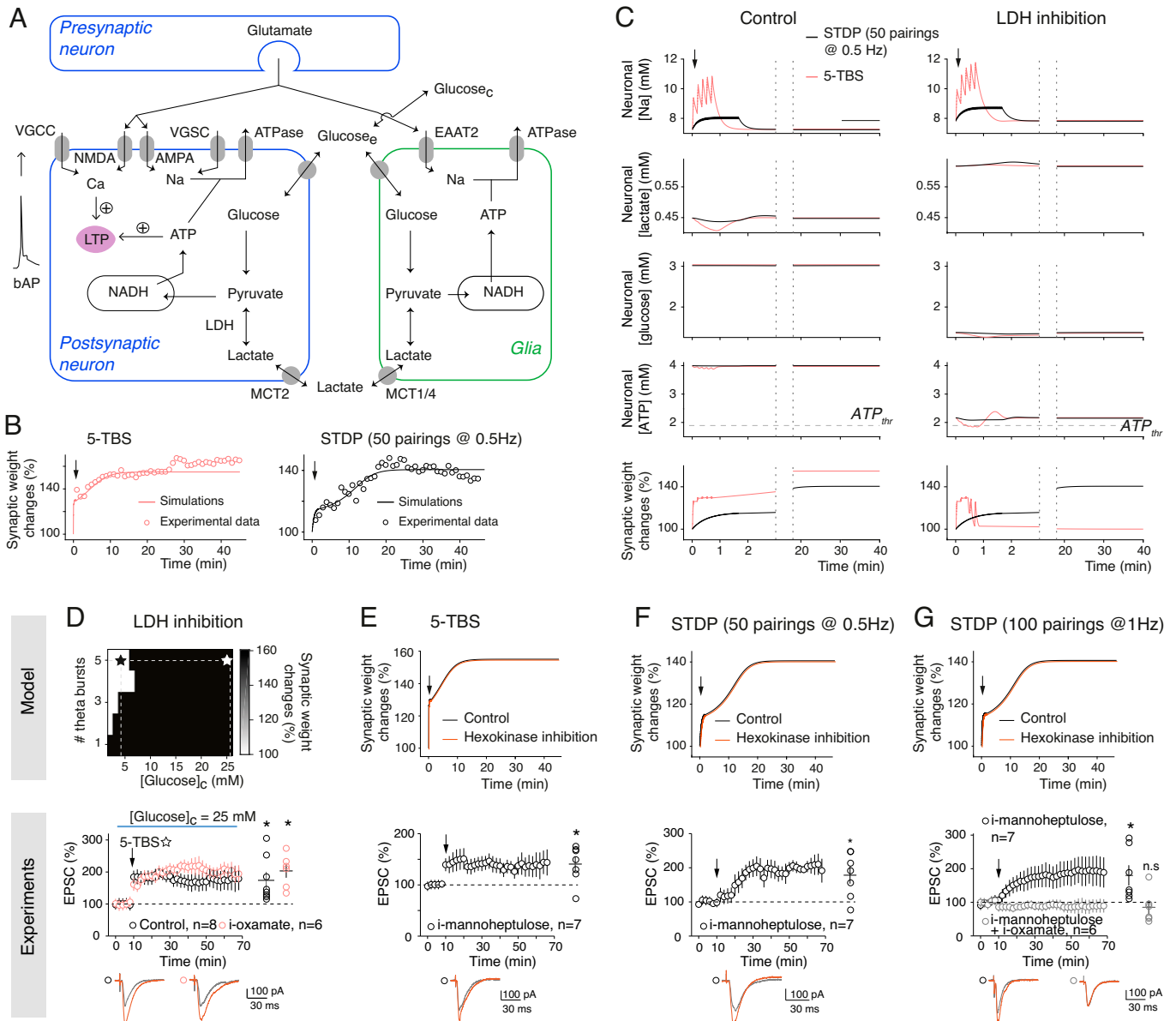
Fig. 2. Confronting mathematical model and experimental data delineates the energetic needs of synaptic plasticity. (*A*) In the model (*Materials and Methods* and *SI Appendix, Supplementary Information for the Mathematical Model, Supplementary Methods and Materials*, and *SI Appendix*, Table S2), the synaptic weight is gated by both neuronal calcium (potentiation) and ATP (depression); VGCC, voltage-gated calcium channel; VGSC, voltage-gated sodium channel; EAAT2, excitatory amino acid transporter-2; AMPA, α-amino-3-hydroxy-5-methyl-4-isoxazolepropionic acid. (*B*) Time course of the synaptic weight in the model (lines) fitted to 5-TBS ($n = 7$) and STDP ($n = 14$; 50 pairings at 0.5 Hz; spike timing = 10 ms) experiments (circles). (*C*) Model prediction for the evolution of neuronal concentrations and synaptic weight with 5-TBS (red) or STDP (black). (*D*) TBS-LTP expression depending on glucose concentration ([Glucose]$_c$) as predicted by the model. Experimentally, 5-TBS induced LTP ($P = 0.0299$, $n = 8$) at a high glucose concentration (25 mM), and this LTP was not impaired by LDH inhibition (i-oxamate; $P = 0.0044$, $n = 6$). (*E*) 5-TBS–LTP expression with hexokinase inhibition (i-mannoheptulose; $P = 0.0230$, $n = 7$). (*F*) Fifty pairings at 0.5 Hz induced STDP-LTP with i-mannoheptulose ($P = 0.0210$, $n = 7$). (*G*) One hundred pairings at 1 Hz induced STDP-LTP with i-mannoheptulose ($P = 0.0436$, $n = 6$). When neuronal glycolysis and lactate conversion into pyruvate were inhibited with coapplied i-mannoheptulose and i-oxamate, 100 pairings did not induce plasticity ($P = 0.5297$, $n = 6$). Representative traces show 15 EPSCs averaged during baseline (gray) and 45 min (red) after protocols (arrows). All data are represented as mean ± SEM (except in *B* where SEM was omitted for clarity); *, $P < 0.05$; ns, not significant by two tailed *t* test. See *SI Appendix*, Table S3 for detailed data and statistics.

(Fig. 2*B*). We first generated model predictions by varying the number of TBS bursts and predicted that LTP induction by one single burst (1-TBS) would not be dependent on lactate metabolism, whereas LTP induced with at least four bursts (4-TBS) would be, unless performed with high levels of added NADH (Fig. 3*A*). This was validated experimentally because 1-TBS–LTP could be induced with i-oxamate (Fig. 3*A*). As for predictions related to STDP, we first varied in silico the number of pairings and predicted that STDP, even for 500 pairings, would remain nondependent on lactate metabolism (Fig. 3*B*). This was demonstrated experimentally because 100 pairings with a single back-propagating action potential (bAP) at 1 Hz induced LTP

in control and with i-oxamate with similar magnitude (Fig. 3*B* and *SI Appendix*, Table S3). This was confirmed in mice where i-oxamate prevented 5-TBS–LTP but not LTP induced by STDP with 100 pairings (*SI Appendix*, Fig. S5).

We next varied the number of bAPs per STDP pairings and tested the impact of one additional bAP, that is, going from one to two bAPs per STDP pairing. Two-photon imaging of dendritic spines and shafts of CA1 pyramidal cells showed that the calcium transient triggered by two bAPs was roughly two-fold compared to one bAP (*SI Appendix*, Fig. S6), a feature reproduced by the model (*SI Appendix*, Fig. S2*B*). For plasticity induction, we kept constant the overall number of postsynaptic
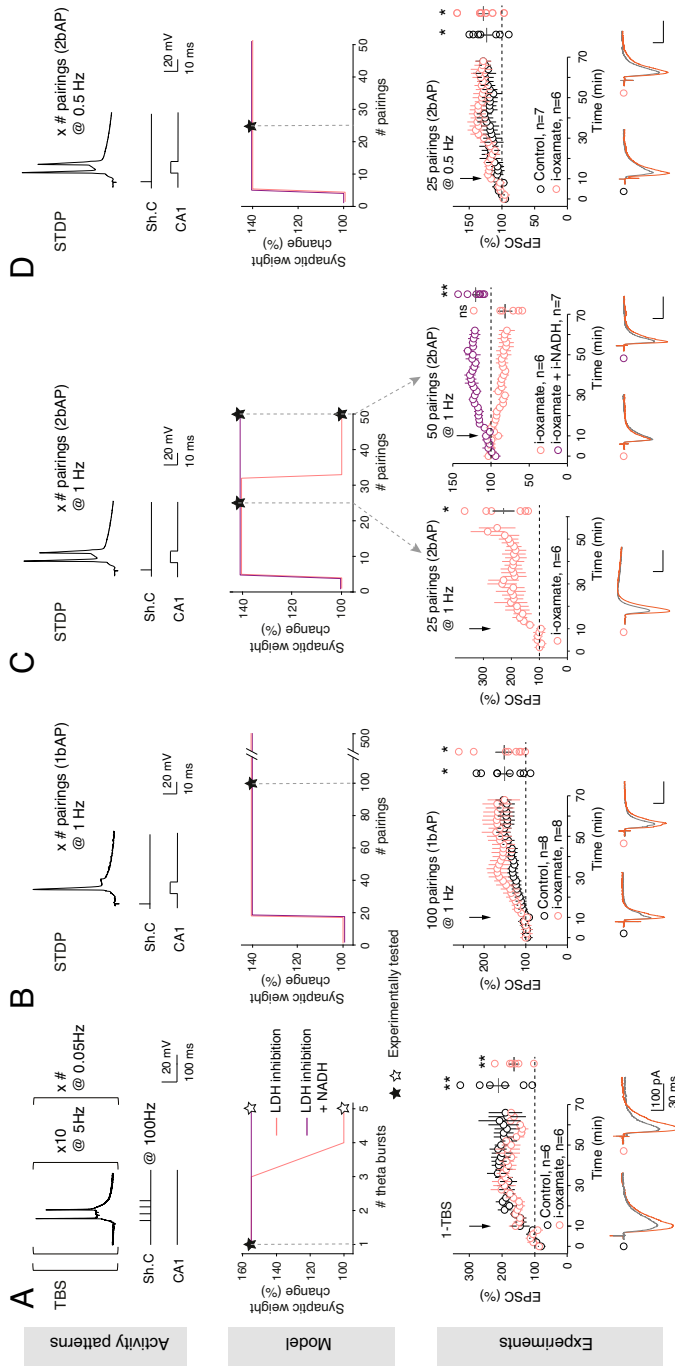
Fig. 3. Dependence on lactate for LTP expression is activity pattern linked. (A) Lactate-dependent TBS-LTP depends on the number of TBS (*Left*, protocol). The model predicts that TBS-LTP is dependent on the lactate pathway from 4-TBS, as demonstrated experimentally with LTP induced by 1-TBS ($P = 0.0229$, $n = 6$), which was not impaired by i-oxamate ($P = 0.0109$, $n = 6$). (B) STDP-LTP induced by 20 to 500 pre/post pairings at 1 Hz with a single bAP/pairing can be induced under LDH inhibition as predicted by the model and demonstrated experimentally with LTP induced by 100 pairings at 1 Hz under control ($P = 0.0191$, $n = 8$) or LDH inhibition ($P = 0.0391$, $n = 8$) conditions, with similar magnitude ($P = 0.9836$). (C) STDP-LTP induced by pairings at 1 Hz with two bAPs/pairing is dependent on LDH activity from 30 pairings, as predicted by the model and demonstrated experimentally with i-oxamate, which prevented LTP expression by 50 ($P = 0.0956$, $n = 6$), but not 25 ($P = 0.0216$, $n = 6$), pairings with two bAPs. Intracellular coapplication of i-oxamate and i-NADH rescued STDP-LTP ($P = 0.0061$, $n = 7$), as predicted by the model. (D) STDP-LTP induced by pairings at 0.5 Hz with two bAPs/pairing ($P = 0.0369$, $n = 7$) can be induced under LDH inhibition ($P = 0.0309$, $n = 6$), as predicted by the model and demonstrated experimentally with LTP induced by 25 pairings with two bAPs/pairing, which is not impaired with i-oxamate. Black stars indicate the experimental conditions tested. Representative traces show 15 EPSCs averaged during baseline (gray) and 45 min (red) after protocol (arrows). All data are represented as mean ± SEM; *, $P < 0.05$; ns, not significant by two tailed t test. See *SI Appendix*, Table S3 for detailed data and statistics.

stimulations, maintaining a total of 100 pairings (100 pairings with one bAP versus 50 pairings with two bAPs) and the same frequency (1 Hz). The model predicted that shifting from one to two bAPs would render STDP lactate dependent if more than 30 pairings were used (Fig. 3C).

Experimentally, with i-oxamate, LTP was induced by 25 pairings at 1 Hz with two bAPs, while no plasticity was detected for 50 pairings (with two bAPs), and adding i-NADH to i-oxamate rescued LTP expression, in agreement with model prediction (Fig. 3C). These observations illustrate that the on-demand fueling is highly sensitive to the activity patterns on either side of the synapse because a variation from one to two bAPs was sufficient to render the lactate pathway necessary for LTP expression.

We finally tested whether the number and frequency of pairings matters. To do so, we kept two bAPs per pairing and decreased the number and frequency of pairings twofold to compare this condition with the STDP paradigm used in Fig. 1, that is, 50 postsynaptic stimulations overall (50 pairings with one bAP versus 25 pairings with two bAPs, both at 0.5 Hz) (Fig. 3D). The model predicted that under these conditions, LTP would be induced and would not depend on lactate. Experimentally, we found that 25 pairings with two bAPs (at 0.5 Hz) induced LTP, and that this LTP was still observed with i-oxamate (Fig. 3D). Therefore, the dependence on glucose versus lactate metabolism precisely scales with the activity patterns used to induce plasticity; glia-derived lactate is required for sustained activity-dependent plasticity, and neuronal glycolysis is sufficient for plasticity induced by lower synaptic activity.

Inhibition of LDH Impairs OiP but not NOR Learning. Because synaptic plasticity is a major substrate for learning and memory (31), we next tested whether lactate dependence scales with learning of recognition memory tasks with increasing cognitive loads. For this purpose, we chose two single-trial tasks involving the hippocampus and perirhinal cortex, which differ by their difficulty level; the OiP task (with four objects) is more challenging and requires a higher cognitive load than the NOR task (with two objects). These tasks were similarly structured into three phases conducted at a 1-d interval: 1) habituation phase in the empty arena, 2) familiarization phase in the presence of two (NOR) or four (OiP) objects, and 3) test in which recognition of new (NOR) or exchanged objects (OiP) was assessed. Rats were injected bilaterally via cannulas implanted just above the CA1 layer with saline or oxamate (50 mM) solutions 45 min before starting the familiarization phase (Fig. 4).

For NOR with two objects (A and B), rats injected with saline ($n = 9$) or oxamate ($n = 10$) performed similarly (Fig. 4 A–O). Indeed, rats spent more time during the test phase around the new object when considering the time per object and the preference index. We ensured that there was no significant preference for object A or B during familiarization because rats (injected in the CA1 with saline or oxamate solutions) spent similar amounts of time exploring objects A and B (*SI Appendix*, Fig. S7A). Similar results were found regardless of whether the familiarization and test phases were achieved with AA/AB ($n = 4$ and 5 rats in saline and oxamate, respectively) or BB/BA ($n = 5$ and 5 rats in saline and oxamate, respectively) object combination (Fig. 4 A–C and *SI Appendix*, Table S4). Indeed, rats detected novelty under saline and oxamate conditions as indicated by the time
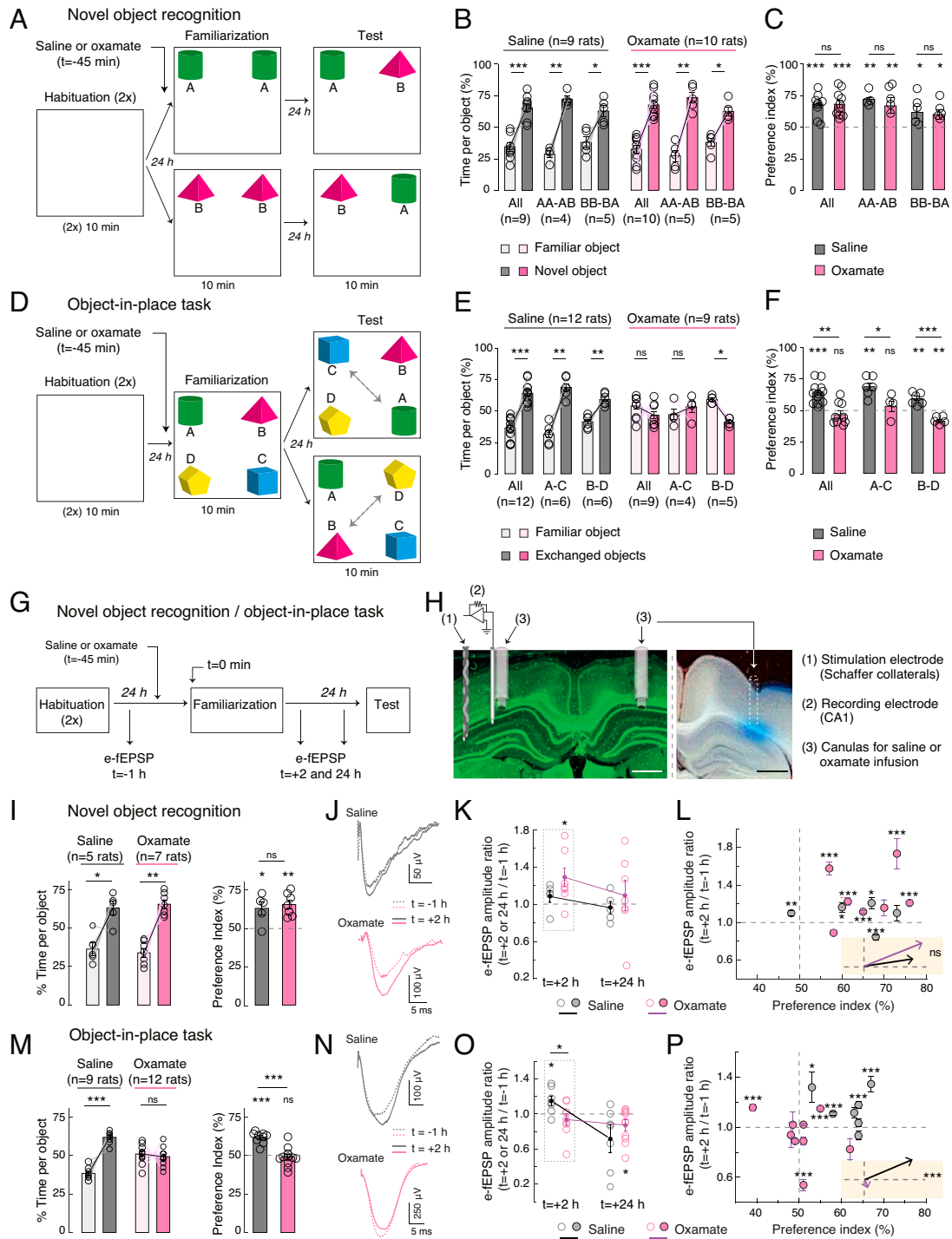
Fig. 4. Inhibition of LDH impairs OiP and associated LTP but not NOR learning. (*A–F*) NOR and OiP tasks were similarly structured into three phases conducted at a 1-d interval: 1) habituation phase in the empty arena, 2) familiarization phase in the presence of two (NOR) or four (OiP) objects, and 3) test in which recognition of new (NOR) or exchanged objects (OiP) was assessed. Rats were injected bilaterally via cannulas implanted just above the CA1 layer with saline or oxamate (50 mM) solutions 45 min before starting the familiarization phase. (*A–C*) NOR task with two objects. (*A*) Experimental setup. Rats were divided in two subgroups exposed to A-A and then A-B or B-B and then B-A during familiarization and test phases, respectively. (*B* and *C*) Rats injected in the CA1 with saline or oxamate (50 mM) spent equally more time exploring the novel object (saline: $P = 0.0007$, $n = 9$; oxamate: $P = 0.0003$, $n = 10$; saline versus oxamate: $P = 0.8126$) as assessed by the time per object (*B*) and the preference index (*C*). LDH inhibition did not impair novelty detection. (*D–F*) OiP task with four objects. (*D*) Rats were exposed to A-B-C-D objects during familiarization and were divided in two subgroups experimenting A-C or B-D exchanged-object for test. (*E* and *F*) Saline-injected rats spent more time exploring the exchanged objects, whereas oxamate-injected rats explored equally all objects (saline: $P < 0.0001$, $n = 12$; oxamate: $P = 0.2500$, $n = 9$; saline versus oxamate: $P = 0.0002$). LDH inhibition impaired the ability of rats to detect place-exchanged objects. (*G–P*) e-fEPSP recordings during NOR and OiP tasks. (*G*) Experimental setup. (*H*) Microphotographs showing cannulas and stimulation/recording electrode locations and diffusion area. (Scale bars, 1 mm.) Chronic stimulating and recording electrodes were placed in Schaffer collaterals and the CA1, respectively, in rats equipped bilaterally with cannulas for saline or oxamate infusion. (*I–P*) In vivo synaptic plasticity during NOR and OiP. e-fEPSPs were recorded before familiarization (baseline) and 2 and 24 h after familiarization to determine synaptic changes in relation to behavior. (*I–L*) NOR behavioral performance (*I*) with related e-fEPSPs showing LTP after 2 h but not after 24 h in saline- and oxamate-injected rats (*J–L*); averaged vectors show similar trends ($P = 0.412$) (*L*). (*M–P*) OiP behavioral performance (*M*) with related e-fEPSPs show LTP in saline-injected but not in oxamate-injected rats 2 h after familiarization (*N–P*); averaged vectors show differences between saline- and oxamate-injected rats ($P < 0.001$) (*P*). All data represent mean ± SEM; *, $P < 0.05$; **, $P < 0.01$; ***, $P < 0.001$; data were analyzed by two-tailed t test. See *SI Appendix*, Table S4 *A–D* for detailed data and statistics.

per object (Fig. 4*B*) and by preference index (Fig. 4*C*) in both AA/AB and BB/BA object combinations.

We next subjected rats to the OiP task (Fig. 4 *D–F*): saline- or oxamate-injected rats (*n* = 12 and 9, respectively) were left for familiarization with four different objects (A, B, C, and D) for which they did not show preference (*SI Appendix*, Fig. S7*B*), and then for the test phase, two of the four objects were place exchanged (from ABCD to CBAD or to ADCB). We found that rats injected with saline spent more time around the exchanged objects, whereas rats injected with oxamate did not notice the exchange because they continued exploring equally the four objects (Fig. 4 *D–F* and *SI Appendix*, Table S4*B*). Similar results were found regardless of whether the familiarization and test phases were performed with ABCD/CBAD (*n* = 6 and 4 rats in saline and oxamate, respectively) or ABCD/ADCB (*n* = 6 and 5 rats in saline and oxamate, respectively) object exchange combination.

Therefore, when conversion of lactate into pyruvate was impaired during familiarization, rats still succeeded in NOR but not in the more challenging OiP task.

Inhibition of LDH Impairs OiP-Induced LTP but not NOR-Induced LTP. We further examined in NOR and OiP tasks whether synaptic plasticity occurred with CA1 hippocampal infusion of saline or oxamate in relation to behavioral performance (Fig. 4 *G–P* and *SI Appendix*, Fig. S7 *C–G* and Tables S4 *A–D*). Synaptic weights were evaluated in vivo by monitoring evoked-field excitatory postsynaptic potentials (e-fEPSPs) at synapses between Schaffer collaterals and CA1 pyramidal cells in behaving rats. To do so, we placed chronic stimulating and recording electrodes in Schaffer collaterals and CA1, respectively, in rats equipped bilaterally with cannulas for saline or oxamate infusion (Fig. 4*H*). We first ensured that this set of rats performed in NOR and OiP similarly as mentioned earlier. In detail, rats infused with saline (*n* = 5) or oxamate (*n* = 7) detected novelty in NOR task (AA-AB) (Fig. 4*I* and *SI Appendix*, Table S4*A*). Regarding the OiP task, rats subjected to saline (*n* = 9) were able to detect novelty, whereas rats infused with oxamate (*n* = 12) did not (ABCD/ADCB) (Fig. 4*M* and *SI Appendix*, Table S4*B*). To determine plasticity expression, e-fEPSPs were monitored before (*t* = −1 h before saline or oxamate injection) and after (*t* = +2 and +24 h) the familiarization phase (Fig. 4 *J–P* and *SI Appendix*, Fig. S7 *C–G*).

In the NOR task, LTP of e-fEPSPs dominated at *t* = +2 h in both saline- and oxamate-injected rats (*n* = 5 and 7, respectively) and is followed by a scaled reduction of synaptic weights at *t* = +24 h (as shown by the positive correlation between plasticities at *t* = +2 and +24 h), leading, on average, to no plasticity at *t* = +24 h (Fig. 4 *J* and *L* and *SI Appendix*, Fig. S7 *C–G* and Table S4*C*). The behavioral and plasticity profiles were similar between saline- and oxamate-injected rats, as illustrated by the average vectors considering the preference index and plasticity at *t* = +2 h after familiarization (Fig. 4*L* and *SI Appendix*, Fig. S7*F* and Table S4*D*).

A different picture was obtained in the OiP task. e-fEPSPs exhibited LTP at *t* = +2 h in saline-injected rats but not in oxamate-injected rats (Fig. 4*O*). More precisely, when considering e-fEPSP plasticity at 2 h after familiarization in relation to behavioral performance, all saline-injected rats detected exchanged objects, and four of seven displayed LTP, whereas among the 78% (seven of nine) of the oxamate-injected rats that did not detect the exchange, only one showed LTP, while the others exhibited an absence of plasticity or long-term depression (LTD). This is also illustrated by the difference

between averaged vectors (Fig. 4*P* and *SI Appendix*, Table S4*D*). Monitoring of the synaptic weights 24 h after familiarization showed similar plasticity pictures for saline- and oxamate-injected rats (*n* = 9 and 12, respectively), that is, LTD or the absence of plasticity despite distinct preference indexes (*SI Appendix*, Fig. S7 *E and G* and Table S4*D*).

In conclusion, rats detecting novelty in the OiP task displayed LTP after the familiarization phase, whereas oxamate-injected rats, which were not able to detect novelty, did not show LTP. Therefore, learning novelty in a challenging memory task (OiP) requires lactate-dependent LTP, while glucose-dependent LTP can be sufficient to learn a less demanding cognitive task (NOR).

Discussion

Here, we show that scaling of computational and cognitive loads requires the metabolism of astrocytic glycogen-derived lactate to match the energetic requirements of sustained neural activity patterns and high cognitive load. For less demanding plasticity and learning paradigms, glucose suffices as an energy substrate. We thus reconcile conflicting views concerning the involvement of lactate versus glucose in synaptic plasticity (11, 26, 27, 32). The two pools of energy substrates (glucose and lactate) can be distinctly allocated on demand (33–37) in qualitative (activity hotspots) and quantitative (engram levels) manners within the hard limit of the global energy availability of cellular metabolism (38, 39). We delineated the domains of activity pattern for which LTP expression requires glucose and/or lactate metabolism and their borders defined by the elementary elements of neural computation, that is, the rate and timing codes. This is particularly illustrated by the fact that variation of a single bAP was sufficient to shift the LTP dependency from glucose to lactate.

Physiologically, lactate in the brain can be formed through two metabolic pathways that correspond to two forms of the astrocyte–neuron lactate shuttle, glycogenolysis and glutamate-stimulated glucose uptake into astrocytes (7, 11). Glycogenolysis in astrocytes is promoted by neuromodulators, such as noradrenaline and vasoactive intestinal peptide (7, 23). The glia-derived lactate, as well as neuronal glycolysis, could thus be triggered after extracellular potassium changes as low as ∼200 μM, according to theoretical estimations of the potassium efflux upon a single action potential (40), consistent with the demonstrated glycogenolytic action of potassium (41–43). Interestingly, noradrenaline is released from fibers in the cortex and hippocampus during task-relevant stimuli, optimizing behavioral performance (44). The firing of the locus coeruleus, where noradrenaline-containing cell bodies are localized, renders neurons in the cortex and hippocampus more responsive to a broad spectrum of stimuli, including behavioral attentional states (44, 45) involved in plasticity and learning. In the context of the observations presented here, it is worth noting that glycogenolysis triggered by activation of beta2 receptors selectively localized on astrocytes is necessary for memory consolidation (16).

Increased energetic demands on astrocytes such as glutamate uptake, one of the main functions of astrocytes, stimulates glucose uptake and the activation of its metabolism through aerobic glycolysis, resulting in lactate production (10). One may therefore wonder which one of the two forms of the astrocyte–neuron lactate shuttle is mobilized during the higher energy-demanding plasticity loads described in this article. The role of glycogen-derived lactate in memory consolidation is now well established (14–16). Recent modeling data show that the glycogenolysis-derived lactate evoked by a glycogenolytic neuromodulator such as noradrenaline (23)

operates with much shorter time constants than the glutamate uptake–triggered one (46).

The demonstration that under conditions of glycogenolysis inhibition, lactate, but not glucose, allows sustained electrical activity (9), fear, or spatial learning (14–16) (that involves high perceptual load) is in line with our results. Also, a decrease in lactate production mediated by mitochondrial cannabinoid type-1 receptor activation in astrocytes alters social behavior in a lactate-reversible manner (47). By contrast, fast-learning engrams originating from light activity patterns (48) could emerge even in the absence of lactate metabolism, with glucose as the main energy substrate.

Our mathematical model predicts that, with oxamate, NADH levels during TBS are larger than during STDP, although less than in control conditions, that is, without LDH inhibition: NADH(STDP + oxamate) < NADH(TBS + oxamate) < NADH(TBS or STDP in control). Because TBS + oxamate is the only condition where LTP is suppressed, we concluded that a simple control of LTP by the level of NADH is unlikely. The dynamics of cytosolic ATP levels were more compatible with a simple gating mechanism because ATP levels in the model were found especially low with TBS + oxamate and much larger for STDP + oxamate or under control conditions (TBS or STDP without oxamate). ATP is usually believed to be tightly regulated in neurons (2, 3, 7), so our model prediction that oxamate causes a twofold decrease of cytosolic ATP at rest is unexpected. We cannot rule out that the metabolite that limits TBS-LTP with oxamate is not ATP but one of its less tightly regulated metabolites or binding partners and one that the model would not account for (ATPases or other ATP-dependent enzymes or channels, for instance). Continuous measurements of cytosolic neuronal ATP/ADP and NADH/NAD$^+$ ratios during TBS or STDP, with and without oxamate, would allow testing our hypothesis. However, to our knowledge, single-cell ATP monitoring in neurons during LTP protocols is still an experimental challenge in brain slices. In any case, the model prediction of depotentiation when ATP drops below a threshold (Fig. 2C) provides a simple mechanism to link metabolism with the signaling pathways of synaptic plasticity. This simple mechanism endowed the model with strong predictive properties, allowing us to correctly forecast the results of a wide range of experimental conditions (number or frequencies of action potentials and glucose concentration). This advocates in favor of the validity of our hypothesis of an ATP-gated depotentiation.

The tight dependence and sensitivity of neuronal signaling on energy availability renders the brain vulnerable to conditions in which energy delivery or utilization are compromised. This is the case for neurodegenerative diseases, such as Alzheimer's and Parkinson's diseases, amyotrophic lateral sclerosis, and frontotemporal dementia (49–52), as well as for neurodevelopmental disorders, such as glucose transporter-1 deficiency syndrome (53). Pharmacological strategies aimed at boosting brain energy metabolism by acting at specific cellular and molecular targets (e.g., neurons versus glial cells and glycolysis versus glycogenolysis) deserve close attention, as they may provide an original and unifying interventional approach for diseases characterized by cognitive impairment and neurodegeneration.

Materials and Methods

Detailed materials and methods, that is, patch-clamp whole-cell and two-photon recordings in brain slices, behavioral tasks, in vivo electrophysiological recordings in behaving rats, and mathematical models, are included in the *SI Appendix, Supplementary Information for the Mathematical Model* and *Supplementary Materials and Methods*.

Experiments were conducted in male Sprague–Dawley rats (Charles River) P$_{30\ to\ 35\ d}$ for brain slice patch-clamp and two-photon imaging and P$_{7\ to\ 9\ wk}$ for behavioral tasks and in vivo electrophysiology and in C57BL/6 mice P$_{28-35\ d}$ for brain slice electrophysiology (*SI Appendix*, Fig. S5).

Whole-Cell CA1 Pyramidal Neuron Recordings. For whole-cell CA1 pyramidal neuron recordings, transverse hippocampal slices (350 µm thick) were prepared. Signals were amplified with EPC10-2 amplifiers (HEKA Elektronik). Current- and voltage-clamp recordings were sampled at 20 kHz with the Patchmaster v2 × 32 program (HEKA Elektronik). All recordings were performed at 35 °C.

Synaptic Plasticity Induction Protocols. Synaptic responses in CA1 pyramidal cells were evoked by electrical stimulations of Schaeffer's collaterals with concentric bipolar electrodes (Phymep) placed in the stratum radiatum area of the hippocampus, with two paradigms being applied, TBS and STDP.

NOR and OiP tasks. The NOR (two objects) and OiP (four objects) tasks involved three sessions on three consecutive days: habituation (on day 1), familiarization (on day 2), and test (on day 3).

In Vivo Electrophysiology in Behaving Rats during the NOR and OiP Tasks. fEPSPs evoked from Schaffer collateral stimulation (e-fEPSPs) were measured (KJE-1001 system, Amplipex) in the left CA1 over the 3-d behavioral assessment in rats subjected to NOR or OiP tasks.

Mathematical Model. Our model simulates the network of signaling and metabolic reactions occurring in a postsynaptic neuronal terminal and an interacting astrocyte, as shown in Fig. 2A. The postsynaptic weight was modelled using a bistable ordinary differential equation where potentiation is triggered by high intracellular calcium whereas low cytosolic ATP levels cause depotentiation. The level of intracellular calcium depended on the set of channels and pumps illustrated in Fig. 2A, whereas the time course of ATP concentration was estimated using a model of neuron-glia metabolic interactions (30), thus effectively linking metabolism and plasticity. For parameter values of the mathematical model, see *SI Appendix*, Table S2.

Data, Materials, and Software Availability. Computer code for the model is publicly available at GitLab (https://gitlab.inria.fr/hberry/anls_stdp) (54). All other study data are included in the article and/or *SI Appendix*.

Author affiliations: ᵃDynamics and Pathophysiology of Neuronal Networks Team, Center for Interdisciplinary Research in Biology (CIRB), Collège de France, CNRS, INSERM, Université PSL, 75005 Paris, France; ᵇAIStroSight Lab, INRIA, Hospices Civils de Lyon, Université Claude Bernard Lyon 1, 69603 Villeurbanne, France; ᶜUniversity of Lyon, LIRIS UMR5205, 69622 Villeurbanne, France; ᵈBiological and Environmental Sciences and Engineering (BESE) Division, King Abdullah University of Science and Technology (KAUST), 23955-6900 Thuwal, Saudi Arabia; and ᵉBrain Mind Institute, EPFL, 1015 Lausanne, Switzerland

1. E. Bullmore, O. Sporns, The economy of brain network organization. *Nat. Rev. Neurosci.* **13**, 336–349 (2012).
2. J. J. Harris, R. Jolivet, D. Attwell, Synaptic energy use and supply. *Neuron* **75**, 762–777 (2012).
3. S. Li, Z.-H. Sheng, Energy matters: Presynaptic metabolism and the maintenance of synaptic transmission. *Nat. Rev. Neurosci.* **23**, 4–22 (2022).
4. K. Mann, S. Deny, S. Ganguli, T. R. Clandinin, Coupling of activity, metabolism and behaviour across the *Drosophila* brain. *Nature* **593**, 244–248 (2021).
5. D. Tingley, K. McClain, E. Kaya, J. Carpenter, G. Buzsáki, A metabolic function of the hippocampal sharp wave-ripple. *Nature* **597**, 82–86 (2021).
6. C. R. Figley, P. W. Stroman, The role(s) of astrocytes and astrocyte activity in neurometabolism, neurovascular coupling, and the production of functional neuroimaging signals. *Eur. J. Neurosci.* **33**, 577–588 (2011).
7. P. J. Magistretti, I. Allaman, Lactate in the brain: From metabolic end-product to signalling molecule. *Nat. Rev. Neurosci.* **19**, 235–249 (2018).

8. E. R. Zimmer et al., [18F]FDG PET signal is driven by astroglial glutamate transport. Nat. Neurosci. 20, 393–395 (2017).

9. A. Trevisiol et al., Monitoring ATP dynamics in electrically active white matter tracts. eLife 6, e24241 (2017).

10. L. Pellerin, P. J. Magistretti, Glutamate uptake into astrocytes stimulates aerobic glycolysis: A mechanism coupling neuronal activity to glucose utilization. Proc. Natl. Acad. Sci. U.S.A. 91, 10625–10629 (1994).

11. L. F. Barros, B. Weber, CrossTalk proposal: An important astrocyte-to-neuron lactate shuttle couples neuronal activity to glucose utilisation in the brain. J. Physiol. 596, 347–350 (2018).

12. A. Karagiannis et al., Lactate is an energy substrate for rodent cortical neurons and enhances their firing activity. eLife 10, e71424 (2021).

13. A. I. Ivanov et al., Glycolysis and oxidative phosphorylation in neurons and astrocytes during network activity in hippocampal slices. J. Cereb. Blood Flow Metab. 34, 397–407 (2014).

14. A. Suzuki et al., Astrocyte–neuron lactate transport is required for long-term memory formation. Cell 144, 810–823 (2011).

15. L. A. Newman, D. L. Korol, P. E. Gold, Lactate produced by glycogenolysis in astrocytes regulates memory processing. PLoS One 6, e28427 (2011).

16. C. M. Alberini, E. Cruz, G. Descalzi, B. Bessières, V. Gao, Astrocyte glycogen and lactate: New insights into learning and memory mechanisms. Glia 66, 1244–1262 (2018).

17. P. E. Steadman et al., Disruption of oligodendrogenesis impairs memory consolidation in adult mice. Neuron 105, 150–164 (2020).

18. A. L. Kauffman, J. M. Ashraf, M. R. Corces-Zimmerman, J. N. Landis, C. T. Murphy, Insulin signaling and dietary restriction differentially influence the decline of learning and memory with age. PLoS Biol. 8, e1000372 (2010).

19. K. D. Longden, T. Muzzu, D. J. Cook, S. R. Schultz, H. G. Krapp, Nutritional state modulates the neural processing of visual motion. Curr. Biol. 24, 890–895 (2014).

20. C. Murphy-Royal et al., Stress gates an astrocytic energy reservoir to impair synaptic plasticity. Nat. Commun. 11, 2014 (2020).

21. M. Zuend et al., Arousal-induced cortical activity triggers lactate release from astrocytes. Nat. Metab. 2, 179–191 (2020).

22. Z. Padamsey, D. Katsanevaki, N. Dupuy, N. L. Rochefort, Neocortex saves energy by reducing coding precision during food scarcity. Neuron 110, 280–296 (2022).

23. P. J. Magistretti, J. H. Morrison, W. J. Shoemaker, V. Sapin, F. E. Bloom, Vasoactive intestinal polypeptide induces glycogenolysis in mouse cortical slices: A possible regulatory mechanism for the local control of energy metabolism. Proc. Natl. Acad. Sci. U.S.A. 78, 6535–6539 (1981).

24. A. M. Brown, B. R. Ransom, Astrocyte glycogen and brain energy metabolism. Glia 55, 1263–1271 (2007).

25. J. P. Bolaños, A. Almeida, S. Moncada, Glycolysis: A bioenergetic or a survival pathway? Trends Biochem. Sci. 35, 145–149 (2010).

26. C. M. Díaz-García et al., Neuronal stimulation triggers neuronal glycolysis and not lactate uptake. Cell Metab. 26, 361–374 (2017).

27. G. Yellen, Fueling thought: Management of glycolysis and oxidative phosphorylation in neuronal metabolism. J. Cell Biol. 217, 2235–2246 (2018).

28. E. de Tredern et al., Glial glucose fuels the neuronal pentose phosphate pathway for long-term memory. Cell Rep. 36, 109620 (2021).

29. R. Gruetter, K. Ugurbil, E. R. Seaquist, Steady-state cerebral glucose concentrations and transport in the human brain. J. Neurochem. 70, 397–408 (1998).

30. R. Jolivet, J. S. Coggan, I. Allaman, P. J. Magistretti, Multi-timescale modeling of activity-dependent metabolic coupling in the neuron–glia–vasculature ensemble. PLoS Comput. Biol. 11, e1004036 (2015).

31. S. Nabavi et al., Engineering a memory with LTD and LTP. Nature 511, 348–352 (2014).

32. L. K. Bak, A. B. Walls, CrossTalk opposing view: Lack of evidence supporting an astrocyte-to-neuron lactate shuttle coupling neuronal activity to glucose utilisation in the brain. J. Physiol. 596, 351–353 (2018).

33. K. A. Kasischke, H. D. Vishwasrao, P. J. Fisher, W. R. Zipfel, W. W. Webb, Neural activity triggers neuronal oxidative metabolism followed by astrocytic glycolysis. Science 305, 99–103 (2004).

34. J. Chuquet, P. Quilichini, E. A. Nimchinsky, G. Buzsáki, Predominant enhancement of glucose uptake in astrocytes versus neurons during activation of the somatosensory cortex. J. Neurosci. 30, 15298–15303 (2010).

35. P. Mächler et al., In vivo evidence for a lactate gradient from astrocytes to neurons. Cell Metab. 23, 94–102 (2016).

36. I. Ruminot, J. Schmälzle, B. Leyton, L. F. Barros, J. W. Deitmer, Tight coupling of astrocyte energy metabolism to synaptic activity revealed by genetically encoded FRET nanosensors in hippocampal tissue. J. Cereb. Blood Flow Metab. 39, 513–523 (2019).

37. C. N. Hall, M. C. Klein-Flügge, C. Howarth, D. Attwell, Oxidative phosphorylation, not glycolysis, powers presynaptic and postsynaptic mechanisms underlying brain information processing. J. Neurosci. 32, 8940–8951 (2012).

38. D. D. Clarke, L. Sokoloff, "Circulation and Energy Metabolism of the Brain" in Basic Neurochemistry: Molecular, Cellular and Medical Aspects, G. J. Siegel et al., Eds. (Lippincott-Raven, Philadelphia, ed. 6, 1999), vol. 31, chap. 31.

39. M. Bruckmaier, I. Tachtsidis, P. Phan, N. Lavie, Attention and capacity limits in perception: A cellular metabolism account. J. Neurosci. 40, 6801–6811 (2020).

40. M. J. Saetra, G. T. Einevoll, G. Halnes, An electrodiffusive neuron-extracellular-glia model for exploring the genesis of slow potentials in the brain. PLOS Comput. Biol. 17, e1008143 (2021).

41. P. R. Hof, E. Pascale, P. J. Magistretti, K+ at concentrations reached in the extracellular space during neuronal activity promotes a Ca2+-dependent glycogen hydrolysis in mouse cerebral cortex. J. Neurosci. 8, 1922–1928 (1988).

42. C. X. Bittner et al., Fast and reversible stimulation of astrocytic glycolysis by K+ and a delayed and persistent effect of glutamate. J. Neurosci. 31, 4709–4713 (2011).

43. H. B. Choi et al., Metabolic communication between astrocytes and neurons via bicarbonate-responsive soluble adenylyl cyclase. Neuron 75, 1094–1104 (2012).

44. G. Aston-Jones, J. D. Cohen, An integrative theory of locus coeruleus–norepinephrine function: Adaptive gain and optimal performance. Annu. Rev. Neurosci. 28, 403–450 (2005).

45. S. Bouret, S. J. Sara, Reward expectation, orientation of attention and locus coeruleus–medial frontal cortex interplay during learning. Eur. J. Neurosci. 20, 791–802 (2004).

46. J. S. Coggan et al., Norepinephrine stimulates glycogenolysis in astrocytes to fuel neurons with lactate. PLOS Comput. Biol. 14, e1006392 (2018).

47. D. Jimenez-Blasco et al., Glucose metabolism links astroglial mitochondria to cannabinoid effects. Nature 583, 603–608 (2020).

48. C. Piette, J. Touboul, L. Venance, Engrams of fast learning. Front. Cell. Neurosci. 14, 575915 (2020).

49. B. M. Morrison et al., Oligodendroglia have a fundamental role in metabolic support of axons and contribute to neurodegeneration. Nature 487, 443–448 (2012).

50. S. Camandola, M. P. Mattson, Brain metabolism in health, aging, and neurodegeneration. EMBO J. 36, 1474–1492 (2017).

51. S. C. Cunnane et al., Brain energy rescue: An emerging therapeutic concept for neurodegenerative disorders of ageing. Nat. Rev. Drug Discov. 19, 609–633 (2020).

52. D. Pathak, A. Berthet, K. Nakamura, Energy failure: Does it contribute to neurodegeneration? Ann. Neurol. 74, 506–516 (2013).

53. M. Tang, S. H. Park, D. C. De Vivo, U. R. Monani, Therapeutic strategies for glucose transporter 1 deficiency syndrome. Ann. Clin. Transl. Neurol. 6, 1923–1932 (2019).

54. H. Berry, ANLS_STDP. GitLab. https://gitlab.inria.fr/hberry/anls_stdp. Deposited 24 May 2021.

PNAS

Supporting Information for

Lactate supply overtakes glucose when neural computational and cognitive loads scale up

Yulia DEMBITSKAYA, Charlotte PIETTE, Sylvie PEREZ, Hugues BERRY, Pierre J MAGISTRETTI and Laurent VENANCE

Emails for correspondence:

laurent.venance@college-de-france.fr

pierre.magistretti@kaust.edu.sa

hugues.berry@inria.fr

This PDF file includes:

Supporting Information text:
Supplementary Materials and Methods
Supplementary Information for the mathematical model

Supporting Figures and Tables
Figures S1 to S7
Tables S1 to S4

SI references

Supporting Information Text

Supplementary Materials and Methods

Animals
Experiments were conducted in male Sprague Dawley rats (Charles River, L'Arbresle, France) $P_{30-35\ days}$ for brain slice patch-clamp and two-photon imaging, and $P_{7-9\ weeks}$ (weight: 250-300 g) for behavioral tasks and *in vivo* electrophysiology. C57BL/6 mice P_{28-35} days were used for slice electrophysiology (*SI Appendix* Fig. S5). All experimental protocols were approved by the local animal welfare committee (Center for Interdisciplinary Research in Biology Ethics Committee) and EU guidelines (directive 2010/63/EU). Every effort was made to minimize animal suffering and to use the minimum number of animals per group and experiment. Animals were housed in standard 12-hour light/dark cycles and food and water were available *ad libitum.*

Patch-clamp whole-cell recordings in brain slices
Transverse hippocampal slices (350μm-thick) were prepared using a vibrating blade microtome (7000smz-2, Campden Instruments Ltd., UK) in ice-cold cutting solution containing (in mM): 93 N-Methyl-D-glucamine-Cl, 2.5 KCl, 30 NaHCO$_3$, 1.2 NaH$_2$PO4, 20 HEPES, 5 Na-ascorbate, 0.5 CaCl$_2$, 1 MgSO$_4$*7H$_2$O, 25 glucose, 3 Na pyruvate. The slices were transferred to the storage solution containing (in mM): 125 NaCl, 2.5 KCl, 5 glucose, 25 NaHCO$_3$, 1.25 NaH$_2$PO$_4$, 2 CaCl$_2$, 1 MgCl$_2$ with 10 μM pyruvic acid, for one hour at 34°C and then to room temperature. In a subset of experiments (Fig. 2D) storage solution containing 25 mM of glucose was used, as specified. All solutions were saturated with 95% O$_2$ and 5% CO$_2$. For whole-cell recordings from CA1 pyramidal neurons, borosilicate glass pipettes of 3-5 MΩ resistance were filled with (in mM): 127 K-gluconate, 30 KCl, 10 HEPES, 10 phosphocreatine (or 5 as specified in *SI Appendix* Fig. S4), 4 Mg-ATP (or 2 as specified in *SI Appendix* Fig. S4), 0.3 Na-GTP, 0.1 EGTA (adjusted to pH 7.35 with KOH). The composition of the extracellular solution was (mM): 125 NaCl, 2.5 KCl, 5 (or 25 as specified in Fig. 2D) glucose, 25 NaHCO$_3$, 1.25 NaH$_2$PO$_4$, 2 CaCl$_2$, 1 MgCl$_2$ and 10 μM pyruvic acid, through which 95% O$_2$ and 5% CO$_2$ was bubbled. Signals were amplified with EPC10-2 amplifiers (HEKA Elektronik, Lambrecht, Germany). Current- and voltage-clamp recordings were sampled at 20 kHz, with the Patchmaster v2x32 program (HEKA Elektronik). All recordings were performed at 35°C, using a temperature control system (Bath-controller V, Luigs & Neumann, Ratingen, Germany) and slices were continuously perfused at a rate of 2 ml/min.

Synaptic plasticity induction protocols
Synaptic responses in CA1 pyramidal cells were evoked by electrical stimulations of Schaeffer's collaterals with concentric bipolar electrodes (Phymep, Paris, France) placed in *stratum radiatum* area of hippocampus, at a distance exceeding 200 μm from the recording site. Electrical stimulations were monophasic, at constant current (ISO-Flex stimulator, AMPI, Jerusalem, Israel). Currents were adjusted to evoke 100-300 pA EPSCs. Repetitive control stimuli were applied at 0.1 Hz. Recordings were made over a period of 10 min at baseline, and for at least 60 min after the synaptic plasticity induction protocols; long-term changes of synaptic weight were measured in the last 10 min. Experiments were excluded if the mean input and series resistance (Ri and Rs, respectively) varied by more than 20% through the experiment.
Theta-burst stimulation (TBS). TBS of the Schaeffer's collaterals consisted of 10 bursts (single burst: 4 stimuli of 0.2 ms duration at 100 Hz) repeated at 5 Hz. TBS were applied either as a single TBS (1-TBS; Fig. 3A) or repeated 5 times at 0.1 Hz (5-TBS).
Spike-timing-dependent plasticity (STDP) protocols. STDP protocols consisted of pairings of pre- and postsynaptic stimulations separated by a fixed time interval (Δt$_{STDP}$=+10-15 ms, *i.e.* presynaptic stimulation preceded postsynaptic activation) (1,2). Presynaptic stimulations corresponded to Schaeffer's collaterals stimulations and the postsynaptic stimulation of an action potential (AP) evoked by a depolarizing current step (10 ms duration) in the recorded CA1 pyramidal cell. In a subset of experiments (Fig. 3C and 3D), 2 postsynaptic APs were elicited, as specified. Paired stimulations were repeated *n* times at a *f* frequency. In Figure 1 and *SI Appendix* Figure S1, we used STDP with 50 pairings at 0.5 Hz. In Figure 2 and 3, the number of postsynaptic APs (1 or 2), number of pairings (25, 50 or 100) and frequency (0.5 or 1 Hz) were varied.

Patch-clamp data analysis
Off-line analysis was performed with Fitmaster (Heka Elektronik), Igor-Pro 6.0.3 (Wavemetrics, Lake Oswego, OR, USA) and custom-made software in Python 3.0. Statistical analysis was performed with Prism 5.02 software (San Diego, CA, USA). We individually measured and averaged 60 successive EPSCs, comparing the last 10 min of the recording with the 10-min baseline recording in each condition using t-test. In all cases "n" refers to a single cell experiment from a single brain slice. All results are expressed as mean±SEM. Statistical significance was assessed by two-tailed student t-tests (unpaired or paired t-tests) or one-way ANOVA (with Newman-Keuls post hoc test) when appropriate, using the indicated significance threshold (*p*).

Two-photon imaging combined with whole-cell patch-clamp recordings
Morphological tracer Alexa Fluor 594 (50 μM) (Invitrogen, Waltham, MA, USA) and calcium-sensitive dye Fluo-4F (250 μM) (Invitrogen) were added to the intracellular solution. Cells were identified under Scientifica TriM-

Scope II system (LaVision, Germany), with a 60x/1.00 water-immersion objective. Alexa Fluor 594 and Fluo-4F were excited at 830 nm wavelength (femtoseconds IR laser Chameleon MRU-X1; Coherent, UK), and their fluorescence were detected with photomultipliers within 525/50 and 620/60 nm ranges, respectively. Line-scan imaging at 200 Hz was performed to obtain calcium signals in the dendritic shaft and spines and was synchronized with patch-clamp recordings. In each recording, we produced somatic depolarization and monitored maximal Ca2+ elevations to verify linear dependence of Fluo-4F Ca2+ signals (nonlinearity was below 20%) and that Ca2+ transients were below saturation level. The changes in baseline Ca2+ level were monitored as the ratio between the baseline Fluo-4F and Alexa Fluor 594 fluorescence. The cell was discarded for ratio>20%. The dark noise of the photomultipliers was collected when the laser shutter was closed in every recording. One or two bAPs evoked by a depolarizing current step (10 ms) were applied to monitor dendritic calcium transients. Electrophysiological data and calcium transients were analyzed with Fitmaster (Heka Elektronik) and custom-made software in Python 3.0 (https://github.com/calciumfilow/calcium-trace-extractor). The measurements of calcium transient were represented as $\Delta G/R$: $(G_{peak}-G_{baseline})/(R_{baseline}-R_{dark\ noise})$. Baseline Ca2+ signals were represented by baseline G/R, $(G_{baseline}-G_{dark\ noise})/(R_{baseline}-R_{dark\ noise})$, where G is the Fluo-4F fluorescence, and R is Alexa Fluor 594 fluorescence. $G_{baseline}$, $R_{baseline}$ and G_{peak} were obtained from the parameters of the bi-exponential fitting model in each trial and then averaged between 5-6 repetitions for each condition; the bi-exponential fitting was chosen to maximize the fit of the calcium-evoked events and gave better fit quality than single- and triple-exponential fitting. $G_{dark\ noise}$ and $R_{dark\ noise}$ are the dark currents of the photomultipliers. We ensured that $R_{baseline}$ and $G_{baseline}/R_{baseline}$ ratio did not exceed 20% over recording. The statistical significance was tested using a paired or unpaired Student's t-test.

Chemicals
1,4-Dideoxy-1,4-imino-D-arabinitol hydrochloride (DAB) (10µM) and DAB+L-lactate (10mM) were dissolved directly in the extracellular solution. (+)-5-methyl-10,11-dihydroxy-5H-dibenzo(a,d)cyclohepten-5,10-imine (MK801) (1mM), Na-oxamate (6mM), Na-oxamate (6mM) + L-pyruvate (10mM), Na-oxamate (6mM) + K_2NADH (4mM), D-Mannoheptulose (10µM), D-Mannoheptulose (10µM) + Na-oxamate (6mM), were added to intracellular recording solution. Na-oxamate (50mM) was dissolved directly in the saline solution for *in vivo* experiments. All chemicals were purchased from Sigma (Saint-Quentin Fallavier, France) except for MK801 (Tocris, Ellisville, MO, USA). For patch-clamp experiments, drugs were applied intracellularly (noted: i-drugs), ensuring specific intracellular effect in the sole recorded neuron without affecting the neighboring neurons or astrocytes; in few cases (Fig. 1E), drugs were applied extracellularly (noted: e-drugs).

Cannulas implants and *in vivo* microinjections
Under anesthesia with pentobarbital sodium (50 mg/kg i.p.), rats (250–300 g) were placed in a stereotactic apparatus and two holes were drilled to aseptically implant double guide cannulas (26GA, Bilaney, Germany) into dorsal hippocampi bilaterally (stereotaxic coordinates: anteroposterior =-4.0mm from bregma; mediolateral =-2.5mm from midline) (Fig. 4H), secured with dental cement. The two internal cannulas (33GA, Bilaney, Germany) were then inserted within the guide cannulas (dorsoventral =-2.2mm from bone surface). After surgery, 1mg/g i.p. of analgesic agent (Metacam, 1.5mg/ml solution) was administered for 3 days. Rats were allowed to recover from surgery for 7 days before behavioral test beginning. Rats were injected bilaterally through the stainless-steel cannulas 45 min before the familiarization phase of behavioral testing. Cannulas were briefly connected to 10 µL Hamilton syringes by means of polyethylene tubes. Rats were injected with either saline (0.8 mM sterile NaCl) or with Na-oxamate (50 mM) diluted in saline; 1-2 µl per hippocampus using automatic infusion pump at a speed of 0.2 µl/min.

Procedures for novel object recognition (NOR) and object-in-place (OiP) tasks
NOR and OiP tasks were run in a black Plexiglas training arena (100×100cm with 50 cm walls) in a sound-attenuated room with a controlled light intensity of 50 lx. The objects used were made out of plastic (laboratory cylinders and Lego blocks) and were selected to induce comparable attraction (*SI Appendix* Fig. S7A-B). The objects were fixed on the arena floor with a 10 cm distance from the walls. The NOR (2 objects: A and B) and OiP (4 objects: A, B, C and D) tasks involved three sessions upon three consecutive days: habituation (day 1), familiarization (day 2) and test (day 3).
Habituation (NOR and OiP). On day 1, rats were introduced into the empty arena (in its center) for 10 min; this was repeated twice the first day with 4 h intersession interval.
NOR task. For the familiarization session on day 2, the rat was placed in the center of the arena and exposed to two identical objects for 10 min: two objects A for half of the animals and two objects B for another half of the rats. Then, rats were returned to their home cage. For the test session on day 3, the rat was placed back into the center of the arena for object discrimination and were exposed to one familiar object and a novel test object, B for group precedingly exposed to A-A and A for group exposed to B-B, for 10 min.
OiP task. For the familiarization (day 2), the rat was placed in the center of the arena and exposed to four different objects: A, B, C, D, located clockwise as A-B-C-D, for 10 min. For the test session on day 3, the rat

was placed back into the arena for object discrimination and were exposed to the exchanged position of two of the presented objects, C-B-A-D for half of the animals and A-D-C-B for another half, for 10 min.

NOR and OiP performance analysis. Rats were videotaped during familiarization and test sessions. Videos were analyzed and time spent on exploration each object (sniffing or licking) was measured during familiarization and test sessions. For assessing NOR and OiP memory performance, the calculation of object discrimination, the exploration time of the novel object was expressed as percentage of the total exploration time of familiar and novel objects during familiarization and test sessions. Then, we calculated the relative time of exploration per object and the preference index (%) in control (saline-injected rats) and in oxamate (Na-oxamate-injected rats).

In vivo electrophysiology in behaving rats during NOR and OiP task

e-fEPSP were measured in the left CA1 over the 3-day behavioral assessment in rats subjected to NOR (familiarization: A-A and test: A-B) or OiP (familiarization: A-B-C-D and test: C-B-A-D) tasks. A recording wire (stainless steel, 0.005" diameter) was stereotaxically implanted under pentobarbital-ketamine anesthesia (pentobarbital: 30 mg/kg i.p., Ceva Santé Animale, Libourne, France; ketamine: 27.5 mg/kg, i.m., Imalgène, Mérial, Lyon, France) in CA1 stratum radiatum along the guide cannula (anteroposterior: -4.1mm, mediolateral: 2.5, dorsoventral : 3.3), and a bipolar stimulating electrode (2 twisted wires, same as the recording electrode) in the ipsilateral Schaffer collaterals (anteroposterior: -4.4mm, mediolateral: 4.4, dorsoventral : 3.4). The rat body temperature was maintained using at 37°C during surgery. Rats were allowed at least a week of recovery before electrophysiological recordings and behavioral testing. Recordings were performed during 10-15 min in a 24x44cm Plexiglas box, 60 min before familiarization (before the oxamate or saline injection) and, 2 and 24 hours after familiarization. Schaffer e-fEPSPs were amplified, and acquired at 20 kHz using a KJE-1001 system (Amplipex, Szeged, Hungary). Test pulses (150-200 µs, 20-450 µA) were evoked every 30 seconds using a square pulse stimulator and stimulus isolator (Model 2100, AM-Systems, Sequim, WA, USA). Responses were analyzed offline using custom Matlab codes (2019b, The Mathworks, Natick, MA, USA) scripts. Traces was smoothed (linear averaging) over 0.15, 0.25 or 0.5 ms depending on the noise level. Detection of local extrema was performed to define the start and peak of the response, and to measure the e-fEPSP amplitude. Statistical analyses (two-tailed Student t-test) and calculation of plasticity ratio were made on 25 trials. The average baseline of e-fEPSP amplitude obtained at t=-60 min was used to normalize every individual e-fEPSP amplitude at +2 and +24 hours, which were then averaged to obtain the plasticity ratio. The F-statistic and *p*-value associated with the average vectors were obtained from MANCOVA test (two dependent variables: preference index and plasticity ratio; one factor: belonging to the saline- or oxamate-injected rat group). Pearson's correlation coefficients were computed for paired plasticity ratios measured at 2 or 24 hours after familiarization phase.

Histology

After the completion of NOR and OiP experiments, cannulas and recording and stimulation electrodes positions were examined. Rats were anaesthetized (sodium pentobarbital, 150mg/kg i.p.) and transcardially perfused with saline followed by 4% ice-cold paraformaldehyde in 0.1 M phosphate buffer. Brains were extracted, post-fixed in PFA (4% in PBS) for 2 days at 4°C and then cryoprotected in 30% sucrose solution for one week. Brains were cut in coronal 50 µm sections using a cryotome (HM400, Microm Microtech, Francheville, France) and slices were maintained in 0.1 M potassium-PBS (pH=7.4). The sections were Nissl-stained with thionin (Neurotrace 500/525, Thermofischer, Waltham, MA, USA), and images were acquired using a stereozoom microscope (Axiozoom, Zeiss, Oberkochen, Germany) and processed in ImageJ. Only the rats with cannula tips located bilaterally within the dorsal hippocampi were included in the data analysis.

Mathematical model

In the mathematical model, though, parameter calibration imposes to specify which cell type one considers. The vast majority of published models and data on the subject is specific of astrocytes; we opted for astrocytes as glial cells in the model. Our model therefore simulates the network of signaling and metabolic reactions occurring in a postsynaptic neuronal terminal and an interacting astrocyte shown in Figure 2A.

Stimulations. The membrane potential of the postsynaptic compartment V_n is given by:

$$C_m \frac{dV_n}{dt} = -g_L(V_n - E_L) - I_{NMDA} - I_{AMPA} - I_{CaL} + I_{\text{step}} \tag{1}$$

$$\frac{dI_{\text{step}}}{dt} = -\frac{I_{\text{step}}}{\tau_{\text{step}}} + AT \cdot DP_{\max} \sum_i 1_{[t_D^i, t_D^i + DP_{\text{dur}}]}(t) \tag{2}$$

with the indicator function $1_{[a,b]}(x) = 1$ if $x \in [a, b]$, 0 otherwise, t_D^i is the time of the beginning of ith depolarization of the postsynaptic neuron, $DP_{\max}$ is the amplitude of the depolarization current in the postsynaptic neuron and DP_{dur} its duration. τ_{step} is the time step of the step current, AT is the attenuation of the bAP at the postsynaptic compartment and the models for the ionic currents $I_{NMDA}, I_{AMPA}, I_{CaL}$ (Fig. 2A) are given in the Supplementary Information.

STDP 1bAP: For STDP protocols with a single bAP per postsynaptic stimulation, we emulated the bAP by incrementing the postsynaptic potential by a constant value, *i.e.*:

$$V_n\left(t_{bAP1}^{i}{}^{+}\right) = V_n\left(t_{bAP1}^{i}{}^{-}\right) + AT \cdot AP_{\mathrm{amp}} \tag{3}$$

where $t_{bAP1}^{i} = t_D^i + \delta_1$ is the time of the (first) bAP, peaking with a delay δ_1 after the depolarization onset and AP_{amp} is the amplitude of the bAP measured in the soma.

STDP 2bAP: For STDP protocols with two bAPs per postsynaptic stimulation, we added an additional bAP at time $t_{bAP2}^{i} = t_D^i + \delta_1 + \delta_2$ where δ_2 is the delay between the 2 bAPs:

$$V_n\left(t_{bAP2}^{i}{}^{+}\right) = V_n\left(t_{bAP2}^{i}{}^{-}\right) + \alpha AT \cdot AP_{\mathrm{amp}} \tag{4}$$

where α is the attenuation of the second bAP compared to the first. During STDP, we first set the times of each presynaptic stimulation $t_{\mathrm{pre}}^i = t_{\mathrm{pre}}^1 + (i-1)/f$ where t_{pre}^1 is the time of the first presynaptic stimulation (arbitrary) and *f* is the stimulation frequency in Hz. The postsynaptic times are then set according to the spike timing Δt_{STDP}: $t_{bAP1}^i = t_{\mathrm{pre}}^i + \Delta t_{\mathrm{STDP}}$ and $t_D^i = t_{\mathrm{pre}}^i + \Delta t_{\mathrm{STDP}} - \delta_1$

TBS: one presynaptic theta burst is composed of 4 presynaptic stimulations at 100 Hz repeated 10 times at 5 Hz and the frequency of the theta-burst themselves is 0.1 Hz, *i.e.*:

$$t_{\mathrm{pre}}^i = t_{\mathrm{pre}}^1 + \frac{1}{100}\mathrm{mod}(k,4) + \frac{1}{5}\left\lfloor\frac{k}{4}\right\rfloor + \frac{1}{0.1}\left\lfloor\frac{i-1}{40}\right\rfloor$$

where $\lfloor x \rfloor$ denotes the integer part of x, $\mathrm{mod}(x,j) = x - j\lfloor x/j \rfloor$ is its modulo j and $k = \mathrm{mod}(i-1,40)$. On the postsynapse, experiments show that during a presynaptic TBS, the probability for a presynaptic spike to trigger a postsynaptic bAP is circa 0.5, therefore we set $DP_{\mathrm{max}} = 0$ (no postsynaptic current injected in TBS) and set $AP_{\mathrm{max}} = 0$ for odd *i*s.

STDP. The variation of postsynaptic cytosolic calcium concentration is computed as:

$$\tau_{Ca}\frac{\mathrm{d}Ca_n}{\mathrm{d}t} = -Ca_n - \frac{S_m v_n}{F}I_{NMDA} - \frac{S_m v_n}{F}I_{CaL} \tag{5}$$

where $S_m v_n$ is the surface-to-volume ratio of the postsynaptic compartment and F the Faraday constant. In the model, both the cytosolic calcium and ATP concentrations drive a bistable internal signaling state summarized by the state variable $\rho \in [0,1]$ (3):

$$\tau_\rho\frac{\mathrm{d}\rho}{\mathrm{d}t} = -\rho(1-\rho)(\rho^* - \rho) - LTD_{\mathrm{max}}\rho\mathbf{1}_{[LTD_{\mathrm{start}},+\infty[}(Ca_n) + LTP_{\mathrm{max}}(1-\rho)\mathbf{1}_{[LTP_{\mathrm{start}},+\infty[}(Ca_n) - M_{\mathrm{max}}\rho\,\mathbf{1}_{[0,ATP_{\mathrm{Thr}}]}(ATP_n) \tag{6}$$

where ATP_n is the concentration of ATP in the postsynaptic compartment, $LTD_{\mathrm{max}}, LTP_{\mathrm{max}}$ and M_{max} are, respectively, the amplitudes of the calcium-gated LTD and LTP and of the ATP-gated depotentiation and $LTD_{\mathrm{start}}, LTP_{\mathrm{start}}$ and ATP_{Thr} their respective thresholds. ρ^* sets the value of the unstable (intermediate) steady-state of the bistable and τ_ρ the time scale to reach the two stables steady-states $\rho = 0$ and $\rho = 1$. Finally, the synaptic weight is taken an affine function of the signaling state variable: $\quad w(t) = 1 + \beta_\rho\rho(t)$ (7)

Astrocyte-neuron lactate shuttle. To derive the time course of ATP_n in eq. (6) as a function of the pre- and post-synaptic stimulations, we used the model developed by Jolivet *et al* (2015) (4). In both the postsynaptic terminal and a nearby interacting astrocyte (Fig. 2A), the model accounts for glycolysis, *i.e.* the production of pyruvate from glucose with glyceraldehyde-3 phosphate (GAP) and phosphoenolpyruvate (PEP) as intermediates as well as pyruvate formation from lactate by lactate dehydrogenase (LDH). The model also incorporates the production of NADH from pyruvate by the TCA cycle in the mitochondria, resulting ATP production by the electron transport chain as well as NADH shuttling from the cytosol to the mitochondria. Glucose and lactate are exchanged between the cytosol of the two compartments and the periplasmic extracellular medium via transporters, including MCT2 for lactate transport from the periplasmic volume to the postsynaptic compartment. Diffusive transport also occurs between the periplasmic volume and reservoir solutions with fixed concentrations (bath solution or blood capillaries of the slices). In addition, the model accounts for the activity-dependent dynamics of sodium ions in both compartments. Presynaptic stimulations trigger Na influx via EEAT2 channels in the astrocyte and voltage-gated sodium channels (VGSC) and (partly) AMPA receptors in the postsynaptic compartment. Sodium is then pumped back by Na,K-ATPases (ATPase), consuming ATP in the process.

We have implemented the model of Jolivet *et al* (2015) (4) *in extenso*. Our only change has been to substitute the Hodgkin-Huxley equation used for the postsynaptic membrane voltage in (30) by our eq. (1). This made us slightly adapt the maximum conductance for the postsynaptic VGSC, the strength of the effect of the presynaptic stimulation on the astrocyte and the leak conductance. All the remaining of the model, *i.e.* the 28 ODEs and the 80+ remaining parameters were taken unchanged from (4).

Parameter estimation. Coupling the two models (STDP + astrocyte-neuron lactate shuttle) left us with 27 parameters to estimate (*SI Appendix* Table S2). We used a subset of our experimental data (training set), whereas validation was carried out by checking the accuracy of the model output for experimental conditions that were not used in parameter estimation (pharmacology perturbation experiments, changes of extracellular glucose concentrations, different stimulation protocols). See Supplementary Information for a complete description of the model as well as parameter estimation strategy and values.

Code availability: Computer code for the model is publicly available at https://gitlab.inria.fr/hberry/anls_stdp

Supplementary Information Materials and Methods

Mathematical model

Ionic currents of the postsynaptic compartment membrane. The AMPA current was modeled as a double exponential conductance (5):

$$I_{AMPA} = \left[g_{AMPA\text{max}} \sum_i \left(\exp\left(-\frac{t - t_{\text{pre}}^i}{\tau_{AMPA1}} \right) - \exp\left(-\frac{t - t_{\text{pre}}^i}{\tau_{AMPA2}} \right) \right) \mathbf{1}_{[t_{\text{pre}}^i, +\infty[}(t) \right] (V_n - E_{AMPA}) \tag{S1}$$

where t_{pre}^i is the time of the *i*th presynaptic stimulation, $g_{AMPA\text{max}}$ the maximal AMPA conductance and τ_{AMPA1} and τ_{AMPA2} the two-time scales. The NMDAR was also modelled with a double exponential (6):

$$I_{NMDA} = \left[g_{NMDA\text{max}} B \sum_i \left(\exp\left(-\frac{t - t_{\text{pre}}^i}{\tau_{NMDA1}} \right) - \exp\left(-\frac{t - t_{\text{pre}}^i}{\tau_{NMDA2}} \right) \right) \mathbf{1}_{[t_{\text{pre}}^i, +\infty[}(t) \right] (V_n - E_{NMDA}) \tag{S2}$$

where the magnesium block $B = \left(1 + [\text{Mg}^{2+}]/3.57\exp(-0.062V_n) \right)^{-1}$. The VGCC current was modelled after (7) as a high-voltage L-type current:

$$I_{CaL} = g_{Ca\text{L}\text{max}} s^2 u (V_n - E_{Ca}) \tag{S3}$$

with activation and inactivation functions given by:

$$\frac{ds}{dt} = 50(1 - s)\exp\left(\frac{V_n + 29.06}{15.9} \right) - 80s \exp\left(\frac{-V_n - 18.66}{25.6} \right) \tag{S4}$$

and

$$\frac{du}{dt} = (1 - u)\exp\left(\frac{-V_n - 48}{18.2} \right) - u\exp\left(\frac{V_n + 48}{83} \right) \tag{S5}$$

The voltage-gated sodium current was taken from (4): $I_{Na} = g_{Na\text{max}} m_\infty{}^3 h (V_n - E_{Nan})$ (S6)

where the steady-state activation was $m_\infty = \alpha_m/(\alpha_m + \beta_m)$ with $\alpha_m = -0.1(V_n + 33)/[\exp(-0.1(V_n + 33)) - 1]$ and $\beta_m = 4\exp(-(V_n + 58)/12)$ and the inactivation was given by:

$$\frac{dh}{dt} = 0.07(1 - h)\exp\left(\frac{-V_n - 50}{10} \right) - \frac{h}{\exp\left(\frac{-V_n - 20}{10} \right) + 1} \tag{S7}$$

Note that I_{Na} does not contribute to the evolution of the membrane potential in eq.(1) since eq.(1) does not include the spike currents but emulates the bAP using a simple increment of the potential at the spiking time followed by an exponential decay.

Astrocyte-neuron lactate shuttle. We implemented the model of Jolivet *et al* (2015) (4) where S_x denotes the concentration of chemical species S in compartment $x = \{a, n\}$ for astrocyte or postsynaptic neuronal, respectively. We give below a complete depiction of the equations and parameters of the model, but interested readers should refer to the original paper for further specifics.

The cytosolic sodium concentration is given by

$$\frac{dNa_x}{dt} = \frac{S_m v_x}{F} g_{Nax}(E_{Nax} - V_x) - 3S_m v_x k_{\text{pump}x} Na_x \frac{ATP_x}{1 + ATP_x/K_{\text{Mpump}}} + J_{\text{stim}x} \tag{S8}$$

with the Nernst potential $E_{Nax} = RT/F \log(Na_e/Na_x)$, g_{Nax} the leak conductance and $k_{\text{pump}x}$ the maximal rate of the Na-K-ATPase pump in compartment *x*. $J_{\text{stim}x}$ is the sum of sodium influxes triggered by the stimulations. In the postsynaptic compartment: $J_{\text{stim}n} = \frac{S_m v_x}{F}\left(-\frac{2}{3}I_{AMPA} - I_{Na} \right)$ (S9)

6

while in the astrocyte: $J_{\text{stim}a} = 2.25 \times 10^{-5} \times 1500 f \mathbf{1}_{[t_{\text{pre}}^1, t_{\text{pre}}^N]}(t)$ $\qquad$ (S10)

where N is the total number of presynaptic stimulations and f their frequency (4).
Cytosolic glucose concentrations are given by

$$\frac{dGLC_n}{dt} = Tg_{en}\left(\frac{GLC_e}{GLC_e + K_{tg}} - \frac{GLC_n}{GLC_n + K_{tg}}\right) - k_{HKPFKn}\frac{ATP_n}{1+(ATP_n/K_{I,ATP})^4}\frac{GLC_n}{GLC_n + K_g} \qquad (S11)$$

and

$$\frac{dGLC_a}{dt} = Tg_{ca}\left(\frac{GLC_c}{GLC_c + K_{tg}} - \frac{GLC_a}{GLC_a + K_{tg}}\right) + Tg_{ea}\left(\frac{GLC_e}{GLC_e + K_{tg}} - \frac{GLC_a}{GLC_a + K_{tg}}\right) - k_{HKPFKa}\frac{ATP_a}{1+(ATP_a/K_{I,ATP})^4}\frac{GLC_a}{GLC_a + K_g} \qquad (S12)$$

where GLC_e is the extracellular concentration of glucose, i.e. in the pericellular volume, while GLC_c is its – constant - concentration in the large (reservoir) volume of the bath solution and/or the blood vessels. Tg_{xy} is the constant of glucose transport between compartments x and y, k_{HKPFKx} is the maximal rate for the part of glycolysis from hexokinase to phosphofructokinase (lumped as a single equivalent reaction).

Glyceraldehyde-3 phosphate (GAP) concentrations are obtained with:

$$\frac{dGAP_x}{dt} = 2k_{HKPFKx}\frac{ATP_x}{1+(ATP_x/K_{I,ATP})^4}\frac{GLC_x}{GLC_x + K_g} - k_{PGKx}GAP_xADP_x\frac{N - NADH_x^c}{NADH_x^c} \qquad (S13)$$

where k_{PGKx} is the maximal rate for the part of glycolysis from GAP dehydrogenase to enolase, $NADH_x^c$ is the concentration of NADH in the cytosol of compartment x and N is the total concentration of NADH, i.e. the sum of NADH and NAD+ concentration in the cytosol. Phosphoenolpyruvate (PEP) concentration obeys:

$$\frac{dPEP_x}{dt} = k_{PGKx}GAP_xADP_x\frac{N - NADH_x^c}{NADH_x^c} - k_{PKx}PEP_xADP_x \qquad (S14)$$

with k_{PKx} the pyruvate kinase rate in x. Next, the dynamics of pyruvate concentration (PYR) is given by:

$$\frac{dPYR_x}{dt} = k_{PKx}PEP_xADP_x - k_{LDHon x}PYR_xNADH_x^c + k_{LDHoff x}LAC_x(N - NADH_x^c) - $$
$$v_{\text{mito}x}\frac{PYR_x}{K_{Mmito}+PYR_x}\frac{N - NADH_x^m}{N - NADH_x^m + K_{MNADx}} \qquad (S15)$$

Here $k_{LDHon x}$ and $k_{LDHoff x}$ are the forward and reverse rates, respectively, of lactate dehydrogenase (LDH) in compartment x, $NADH_x^m$ is the concentration of NADH in the mitochondrion of x and $v_{\text{mito}x}$ is the maximal rate of the TCA cycle. Lactate (LAC) dynamics is obtained via:

$$\frac{dLAC_n}{dt} = k_{LDHon n}PYR_nNADH_n^c - k_{LDHoff n}LAC_n(N - NADH_n^c) - Tl_{ne}\left(\frac{LAC_n}{LAC_n + K_{tlne}} - \frac{LAC_e}{LAC_e + K_{tlne}}\right) \qquad (S16)$$

where Tl_{xy} is the constant of lactate transport between compartments x and y and LAC_e is the extracellular concentration of lactate, i.e. in the pericellular volume. Likewise, in the astrocyte:

$$\frac{dLAC_a}{dt} = k_{LDHon a}PYR_aNADH_a^c - k_{LDHoff a}LAC_a(N - NADH_a^c) - Tl_{ae}\left(\frac{LAC_a}{LAC_a + K_{tlae}} - \frac{LAC_e}{LAC_e + K_{tlae}}\right) - Tl_{ac}\left(\frac{LAC_a}{LAC_a + K_{tlac}} - \frac{LAC_c}{LAC_c + K_{tlac}}\right) \qquad (S17)$$

where Tl_{xy} is the constant of lactate transport between compartments x and y and LAC_c is the extracellular concentration of lactate in the reservoir volume. Likewise, the concentration of lactose in the pericellular extracellular medium is given by:

$$\frac{dLAC_e}{dt} = \frac{Tl_{ae}}{r_{ea}}\left(\frac{LAC_a}{LAC_a + K_{tlae}} - \frac{LAC_e}{LAC_e + K_{tlae}}\right) + \frac{Tl_{ne}}{r_{en}}\left(\frac{LAC_n}{LAC_n + K_{tlne}} - \frac{LAC_e}{LAC_e + K_{tlne}}\right) - Tl_{ec}\left(\frac{LAC_e}{LAC_e + K_{tlec}} - \frac{LAC_c}{LAC_c + K_{tlec}}\right) \qquad (S18)$$

and that of glucose:

$$\frac{dGLC_e}{dt} = -\frac{Tg_{ea}}{r_{ea}}\left(\frac{GLC_e}{GLC_e + K_{tg}} - \frac{GLC_a}{GLC_a + K_{tg}}\right) - \frac{Tg_{en}}{r_{en}}\left(\frac{GLC_e}{GLC_e + K_{tg}} - \frac{GLC_n}{GLC_n + K_{tg}}\right) + Tg_{ce}\left(\frac{GLC_c}{GLC_c + K_{tg}} - \frac{GLC_e}{GLC_e + K_{tg}}\right) \qquad (S19)$$

with r_{xy} the ratio between the volume of compartment x and that of compartment y. The concentration of cytosolic NADH ($NADH_x^c$) is obtained by integration of:

$$(1-\xi)\frac{dNADH_x^c}{dt} = k_{PGKx}GAP_xADP_x\frac{N - NADH_x^c}{NADH_x^c} - k_{LDHon x}PYR_xNADH_x^c + k_{LDHoff x}LAC_x(N - NADH_x^c) - $$
$$T_{NADHx}\frac{R^-{}_x}{R^-{}_x + M_{cytox}}\frac{R^+{}_x}{R^+{}_x + M_{mitox}} \qquad (S20)$$

where T_{NADHx} is the maximal rate for NADH shuttling from cytosol to the mitochondria sub-compartment, ξ is the relative mitochondria volume, $R^-_x = \frac{NADH^c_x}{N-NADH^c_x}$ and $R^+_x = \frac{N-NADH^m_x}{NADH^m_x}$. For the mitochondrial concentration of NADH, one gets:

$$\xi\frac{dNADH^m_x}{dt} = T_{NADHx}\frac{R^-_x}{R^-_x+M_{cytox}}\frac{R^+_x}{R^+_x+M_{mitox}} + 4v_{\text{mitoin}x}\frac{PYR_x}{K_{Mmito}+PYR_x}\frac{N-NADH^m_x}{N-NADH^m_x+K_{MNADx}} -$$
$$v_{\text{mitoout}x}\frac{O_{2_x}}{K_{O2mito}+O_{2_x}}\frac{ADP_x}{ADP_x+K_{MADPx}}\frac{NADH^m_x}{NADH^m_x+K_{MNADHx}} \tag{S21}$$

where $v_{\text{mitoout}x}$ is the maximal rate of the electron transport chain in x and $O_{2_x}$the oxygen concentration in this compartment. ATP concentration in the postsynaptic compartment is given by:

$$\left(1-\frac{dAMP_n}{dATP_n}\right)\frac{dATP_n}{dt} = -2k_{HKPFKn}\frac{ATP_n}{1+(ATP_n/K_{I,ATP})^4}\frac{GLC_n}{GLC_n+K_g} + k_{PGKn}GAP_nADP_n\frac{N-NADH^c_n}{NADH^c_n} + k_{PKn}PEP_nADP_n -$$
$$J_{ATPasesn} - S_mV_nk_{\text{pump}n}Na_n\frac{ATP_n}{1+ATP_n/K_{Mpump}} + 3.6v_{\text{mitoout}n}\frac{O_{2n}}{K_{O2mito}+O_{2_n}}\frac{ADP_n}{ADP_n+K_{MADPn}}\frac{NADH^m_n}{NADH^m_n+K_{MNADHn}} +$$
$$k_{\text{CKon}n}PCr_nADP_n - k_{\text{CKoff}n}(C-PCr_n)ATP_n \tag{S22}$$

with $J_{ATPasesn}$ a parameter accounting for ATPase activities outside Na-K-ATPases, $k_{\text{CKon}n}$ and $k_{\text{CKoff}n}$ the forward and backward rates of creatine kinase, respectively, and C the total concentration of creatine plus phosphocreatine.

$dAMP_n/dATP_n$, the ratio between deoxyAMP and deoxyATP is computed with $dAMP_x/dATP_x = -1 + 0.5q_{AK} - 0.5\sqrt{u_x} + Aq_{AK}/(ATP_x\sqrt{u_x})$ where q_{AK} is the adenylate kinase equilibrium constant, $A = AMP_x + ADP_x + ATP_x$ is the total adenine nucleotide concentration and $u_x = q_{AK}^2 + 4q_{AK}(A/ATP_x - 1)$. Similarly, the concentration of ADP is computed from that of ATP using $ADP_x = 0.5ATP_x(-q_{AK} + \sqrt{u_x})$.

Now, in the astrocyte, the concentration of ATP is given by:

$$\left(1-\frac{dAMP_a}{dATP_a}\right)\frac{dATP_a}{dt} = -2k_{HKPFKa}\frac{ATP_a}{1+(ATP_a/K_{I,ATP})^4}\frac{GLC_a}{GLC_a+K_g} + k_{PGKa}GAP_aADP_a\frac{N-NADH^c_a}{NADH^c_a} + k_{PKa}PEP_aADP_a -$$
$$J_{ATPasesa} - \frac{3}{4}J_{\text{pump}a0} - \frac{7}{4}S_mV_ak_{\text{pump}a}Na_a\frac{ATP_a}{1+ATP_a/K_{Mpump}} + 3.6v_{\text{mitoout}a}\frac{O_{2a}}{K_{O2mito}+O_{2_a}}\frac{ADP_a}{ADP_a+K_{MADPa}}\frac{NADH^m_a}{NADH^m_a+K_{MNADHa}} +$$
$$k_{\text{CKon}a}PCr_aADP_a - k_{\text{CKoff}a}(C-PCr_a)ATP_a \tag{S23}$$

where phosphocreatine concentrations are given by

$$\frac{dPCr_x}{dt} = -k_{\text{CKon}x}PCr_xADP_x + k_{\text{CKoff}x}(C-PCr_x)ATP_x \tag{S24}$$

Finally, oxygen concentrations are obtained through:

$$\frac{dO_{2x}}{dt} = \frac{PS_{cap}}{v_x}\left(K_{O2}\left(\frac{Hb.OP}{O_{2_c}}-1\right)^{-1/n_h} - O_{2_x}\right) - 0.6v_{\text{mitoout}x}\frac{O_{2_x}}{K_{O2mito}+O_{2_x}}\frac{ADP_x}{ADP_x+K_{MADPx}}\frac{NADH^m_x}{NADH^m_x+K_{MNADHx}} \tag{S25}$$

where PS_{cap}/v_x is the oxygen transport constant from the reservoir to the cells and O_{2_c} oxygen concentration in the reservoir.

Numerical integration. The system of ODEs consisting of eq.(1)-(7) and eq.(S1)-(S25) was integrated using a variable-order adaptive-stepsize stiff solver (ode15s in Matlab®), interrupting integration at every stimulation events (times $t^i_D, t^i_D + DP_{\text{dur}}$, t^i_{bAP1} and t^i_{bAP2} if relevant) to account for the discontinuities of eq.(2-4). The system was first integrated for 2×10^5 seconds in the absence of any electrical stimulation to guaranty that the initial state (before electrical stimulation) is the stable steady-state. After electrical simulation (TBS or STDP), the system was integrated for 45 min. The state of the system 45 min after the stimulation sets the value of the synaptic weight (eq.7) after the stimulation, thus the potential expression of LTP.

Parameter estimation. To calibrate the model, we used the following strategy. All the parameters of equations (S3) to (S25) kept the values set by (4) (*SI Appendix* Table S2) except for $g_{Na\text{max}}$ (eq. S6), g_L(eq.1) and the prefactor of eq.(S10), that were modified as explained below. Therefore, parameter estimation was almost completely restricted to the parameters of eq.(1-7). Together, this represented 27 parameters to estimate (*SI Appendix* Table S2). Parameter values were estimated on a subset of our available experimental data (see below) whereas validation was carried out by checking the accuracy of the model output for experimental conditions that were not used in parameter estimations.

1.	The parameters of the postsynaptic stimulations DP_max, τ_step, AP_amp and α as well as the delays δ_1 and δ_2 and the leak conductance g_L were fitted to the experimental traces of the postsynaptic membrane potential as measured in the soma (*SI Appendix* Fig. S2B). The attenuation factor of the bAP between the soma and the postsynaptic compartment, AT, was set to a value that roughly corresponds to a synapse located at mid-distance between the soma and the dendrite end according to (8) (see their Fig 4D).

2.	$g_{AMPA\text{max}}$, τ_{AMPA1} and τ_{AMPA2} were set to yield EPSPs of 2 mV amplitude, with short onset and a decay time scale around 10 ms, as measured in dendrites by (9). τ_{NMDA1} and τ_{NMDA2} were set to yield a NMDA-component for the calcium influx that rises fast and takes roughly 200 ms to get back to zero and $g_{NMDA\text{max}}$ was fixed so that each presynaptic spike increases the cytosolic calcium level by 0.17 mM at -70 mV (10). $g_{CaL\text{max}}$ was set so that one bAP (on top of the depolarizing current) triggers a calcium influx of 400 nM amplitude at the synapse in the absence of presynaptic stimulation (11). We also checked that with these parameter values, the amplitude of the calcium peak triggered by a postsynaptic stimulation comprising two bAPs is indeed roughly twice the amplitude obtained with a single bAP (*SI Appendix* Fig. S2B) as measured in our experimental setup both in spines and shafts (*SI Appendix* Fig. S6).

3.	In the original model (30), the membrane voltage of the presynaptic compartment is modelled as a Hodgkin-Huxley equation with variable Nernst potentials for Na. Because of the variable Nernst potential, this model exhibits strong spike-frequency adaptation so the postsynaptic neuron quickly ceases to emit spikes after the onset of the stimulation. Since our membrane voltage for the postsynaptic compartment does not exhibit spike-frequency adaptation, we had to adapt a pair of parameters to guaranty that the electrical stimulations employed in the experiments used to calibrate the model by (4) (their Fig. 4A, with experimental data taken from (11) will still yield the correct time course in our model. We therefore adapted the values of $g_{Na\text{max}}$ and the prefactor of eq.(S10) so that the stimulation used in (11) (presynaptic stimulations for 20 sec) yielded in our model the same time-courses for $NADH_a^c$ and $NADH_n^m$ as their experimental measurements (their Fig. 4D). In particular (*SI Appendix* Fig. S2C) this stimulation leads to 1) a dip of $NADH_n^m$ of around -10%, peaking around the end of the effective stimulation, and converging back to baseline after 15-20 min, and 2) a delayed overshoot of $NADH_a^c$ that peaks at approx. +8% roughly 20 min after the end of the stimulation. Those dynamics reproduce previous experimental measurements (33), in both quantitative and qualitative terms.

4.	The parameters related to the dynamics of the synaptic weight were set as follows. The calcium thresholds LTD_start and LTP_start were set so that a "standard" STDP protocol (1 bAP at 1 Hz) triggers LTP for positive spike timings that are not larger than 30 ms and for more than approx. 20 pairings (*SI Appendix* Fig. S2D). The values of LTD_max, LTP_max, ρ^* and β_ρ were fitted on the experimental measurements of the time course of the synaptic weight change for a STDP protocol with 1 bAP, 50 x at 0.5 Hz (Fig. 2B). Note that with 5-TBS, the experimental measurement of the final amplitude of the synaptic weight change was larger than with STDP (Fig. 2B), we thus adapted the value of β_ρ for 5-TBS (but kept the values of LTD_max, LTP_max and ρ^* to those obtained by fitting on STDP 0.5 Hz 50x).

5.	Finally, we fixed the ATP threshold ATP_Thr to a value that allows discriminating between STDP 0.5 Hz 50 pairings (LTP) stimulations and 5-TBS with oxamate (no LTP). In particular, the astrocyte-neuron lactate shuttle model predicts that neuronal ATP, ATP_n, falls below 2 mM for 5-TBS in the presence of oxamate (Fig. 2C), but remains well above 2 mM for 5-TBS in control conditions and STDP 50 pairings at 0.5 Hz (in control and with oxamate). In the absence of experimental data to set the value of M_max, we used a value large enough to cancel LTP for 5-TBS in the presence of oxamate.

Simulation of pharmacological experiments. The action of pharmacological agents was emulated by changing the corresponding parameters to the following values:

1.	*Oxamate*: the forward and backward rate constants of LDH in the postsynaptic neuronal compartment were divided tenfold, i.e. we set $k_{LDH\text{onn}} = 0.723$ mM^{-1}s^{-1} and $k_{LDH\text{offn}} = 0.0720$ mM^{-1}s^{-1}.

2.	*Mannoheptulose:* the forward constant of the HKPFK reaction in the postsynaptic compartment was divided by 1000, *i.e.* we set $k_{HKPFKn} = 0.0504 \times 10^{-3}$ mM^{-1}s^{-1}

3.	*Changes of glucose concentration in the bath:* was emulated by a corresponding change of the glucose concentration in the (constant) reservoir, GLC_c.

4.	*Changes of NADH in the patch pipette:* were emulated by corresponding change of the total NADH+NAD$^+$ concentration *N* in the postsynaptic compartment (while *N* kept its control value of 0.212 mM in the astrocyte).
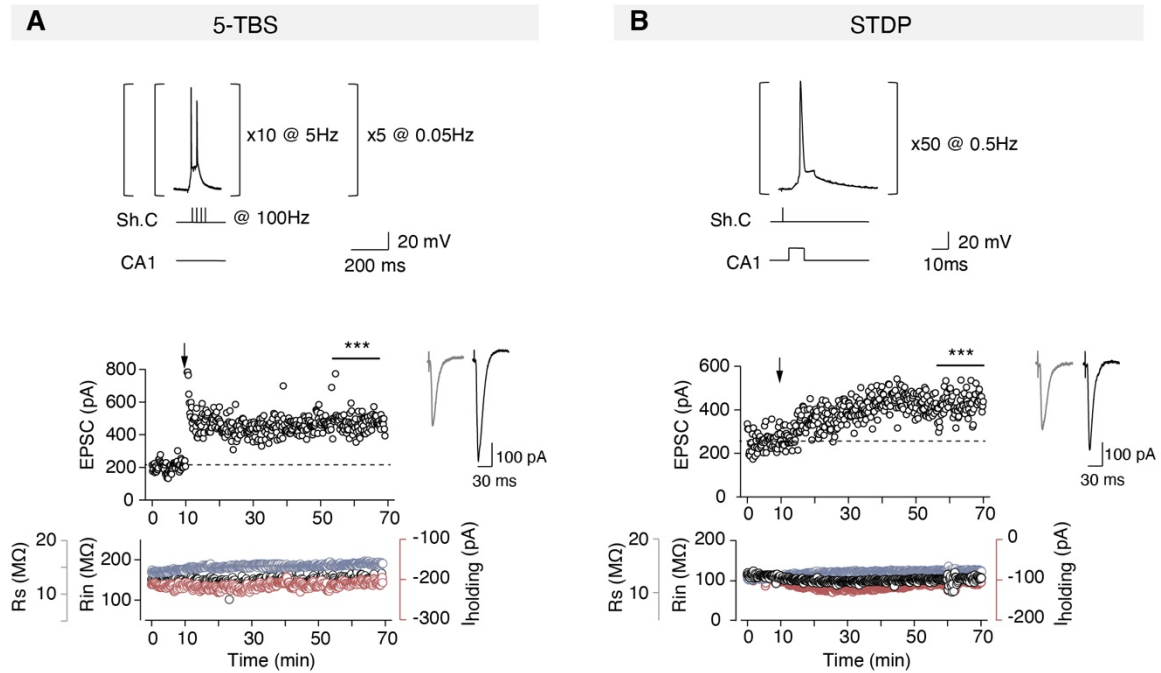
Supporting Figures and Tables

Fig. S1. Representative 5-TBS-LTP and STDP-LTP (50 pairings at 0.5 Hz) (related to the main Figure 1). (**A**) Example of LTP induced by 5-TBS (baseline: 205±4pA, increased by 127%, to 446±6pA, one hour after pairings.). Bottom, time course of Ri (baseline: 145±1MΩ and 50-60 min after pairings: 154±1MΩ; change of 6%), Rs (baseline: 14.14±0.03MΩ and 50-60 min after pairings: 16.31±0.02MΩ; change of 15%) and holding current $I_{holding}$ (baseline: -217±1pA and 50-60 min after pairings: -208±4pA; change of -4%). (**B**) Example of STDP-LTP induced by 50 pre-post pairings (spike timing=-8.7±0.4ms) (the mean baseline EPSC amplitude was 257±5pA before pairings and was increased by ~67% to 430±6pA one hour after pairings). Bottom, time course of Ri (baseline: 110±1MΩ and 50-60 min after pairings: 101±1MΩ; change of -8%), Rs (baseline: 12.72±0.02MΩ and 50-60 min after pairings: 14.05±0.03MΩ; change of 10%) and holding current $I_{holding}$ (baseline: -93±1pA and 50-60 min after pairings: -109±1pA; change of 18%).
Insets correspond to the average EPSC amplitude during baseline (grey traces) and the last 10 min of recording after STDP pairings (red traces). Statistics (student t-test, first vs last 10 min of recording): *** p<0.001.
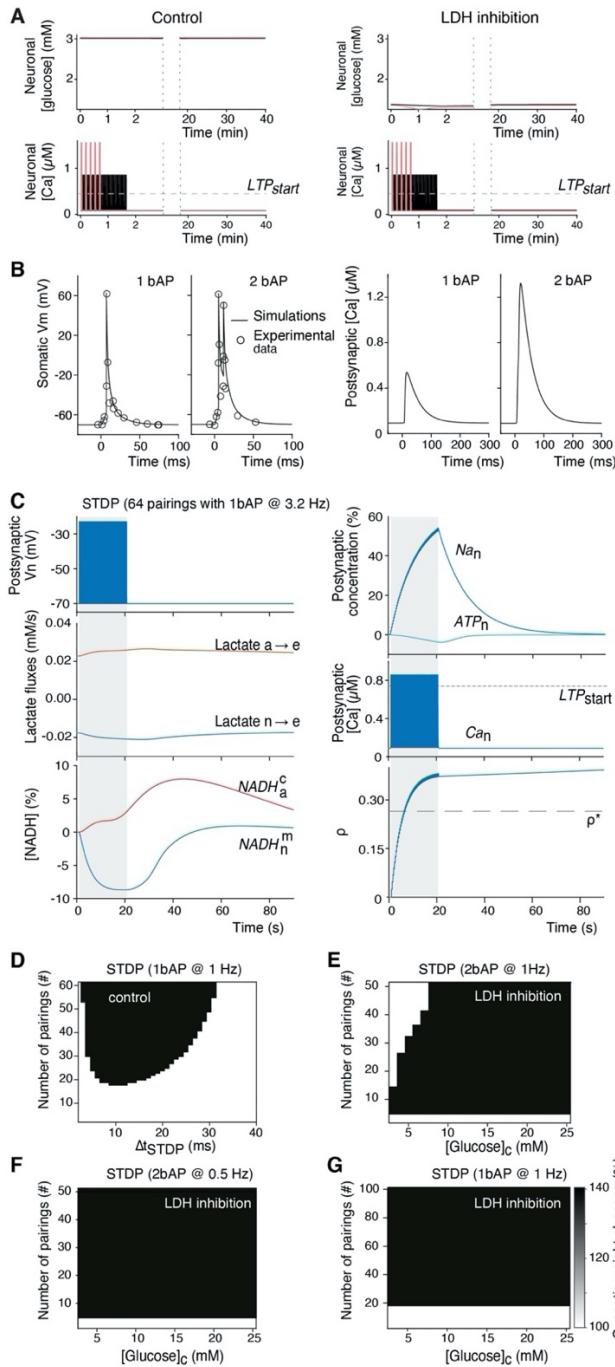
Fig. S2. Model calibration (related to the main Figure 2).
(A) Kinetics of neuronal glucose and calcium with 5-TBS (pink) or light STDP (50 pairings at 0.5Hz, black).
(B) Experimental measurements (circles) and model prediction (line) of the somatic potential with 1 bAP or 2 bAP-stimulations and spike timing 10ms (*left*), together with the resulting calcium transients (*right*). **(C)** After calibration, the glia-neuron lactate shuttle part of the model reproduces experimental data in (*23*) where a 20 sec electrical stimulation of the neurons and astrocytes triggered a decay of neuronal mitochondrial NADH ($NADH_n^m$) by 10% peaking around the end of the stimulation and converging back to baseline 15-20 min afterwards and a delayed overshoot of astrocytic cytosolic NADH ($NADH_a^c$). **(D)** Prediction of synaptic plasticity by the model when the number of pairings and the spike timing vary in STDP (1 bAP at 1Hz) in control conditions. With the color code used, white means no plasticity, while the black zones correspond to LTP (E-G) explore the output of the model with LDH inhibited (oxamate), for STDP with 2 bAPs at 1Hz, 2 bAPs at 0.5Hz, and 1 bAP at 1 Hz, respectively, as a function of the number of pairings and the concentration of glucose in the bath solution.
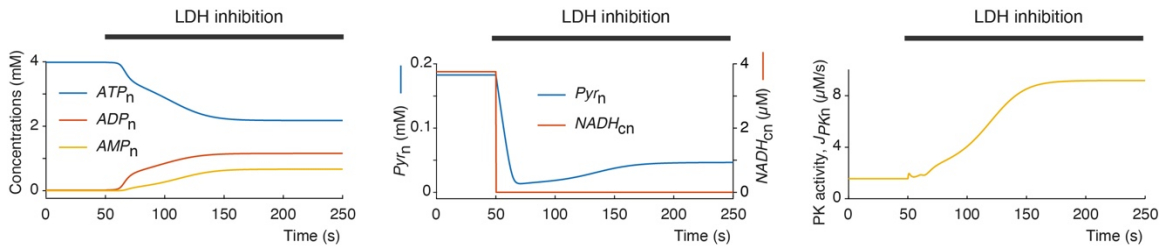
11

Fig. S3. Model prediction of the effects of LDH inhibition on neuronal ATP levels (related to Figure 2).
The model is initiated at time $t=0$ in control conditions. In control ($t< 50s$), ATP makes up roughly the totality of the 4 mM total adenosine phosphate concentration (*top*), the stationary level of pyruvate (Pyr_n) and cytosolic NADH ($NADH_{cn}$) in the neuron is large (*middle*), and neuronal glycolysis is low, as witnessed by the low activity of pyruvate kinase, PK (*bottom*). Oxamate addition in the neuron cytosol at $t=50$ sec rapidly switches the neuron to an oxidized redox state with a close to total depletion of cytosolic NADH. As a result, the ATP level drops well below 4 mM. Oxamate addition also results in neuronal glycolysis, as illustrated by the increase of pyruvate kinase activity. This restores significant levels of neuronal pyruvate and stabilizes ATP to roughly 50% of the total adenosine phosphate, *i.e.* slightly above 2 mM.
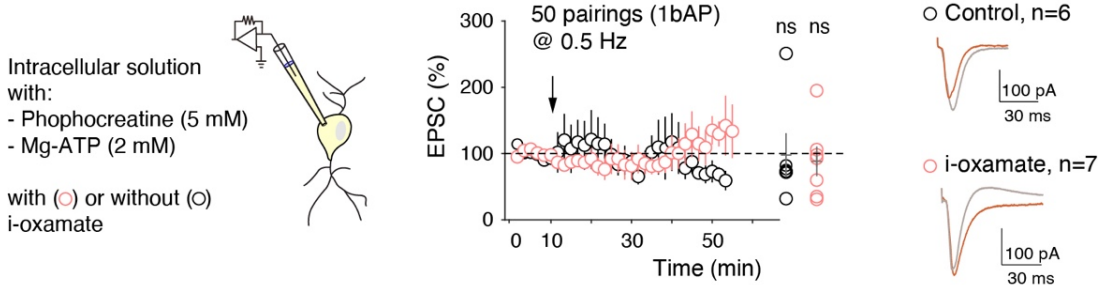
Fig. S4. STDP is prevented with low intracellular ATP (2 mM) and phosphocreatine (5 mM) (related to Figure 2).
Averaged time-course of the synaptic weight and EPSC amplitudes 45-55 min after STDP. When intracellular solution contained 2 mM of ATP and 5 mM phosphocreatine, LTP was not observed after STDP protocol in control or i-oxamate conditions. Only one significant LTP could be induced in control and i-oxamate conditions out of 6 and 7 cells, respectively. All data: mean±SEM. ns: not significant by two tailed *t*-test. See *SI Appendix* Table S3 for detailed data and statistics.
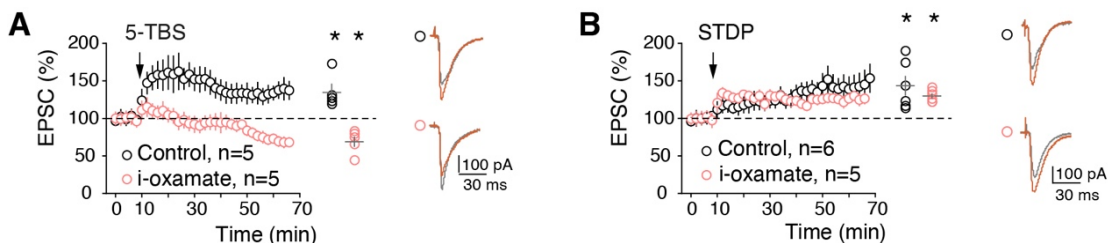
Fig. S5. LDH inhibition prevents 5-TBS-LTP and left unaffected STDP-LTP in adult mice.
Averaged time-course of the synaptic weight and EPSC amplitudes 50-60 min after 5-TBS or STDP in adult mice. Intracellular inhibition of LDH with i-oxamate show distinct effects on 5-TBS and STDP expression since 5-TBS did not induce plasticity whereas STDP triggered a potent LTP. Representative traces: 15 EPSCs averaged during baseline (grey) and 60 min (red) after protocols (arrows).All data: mean±SEM. *p<0.05; ns: not significant by two tailed *t*-test. See *SI Appendix* Table S3 for detailed data and statistics.
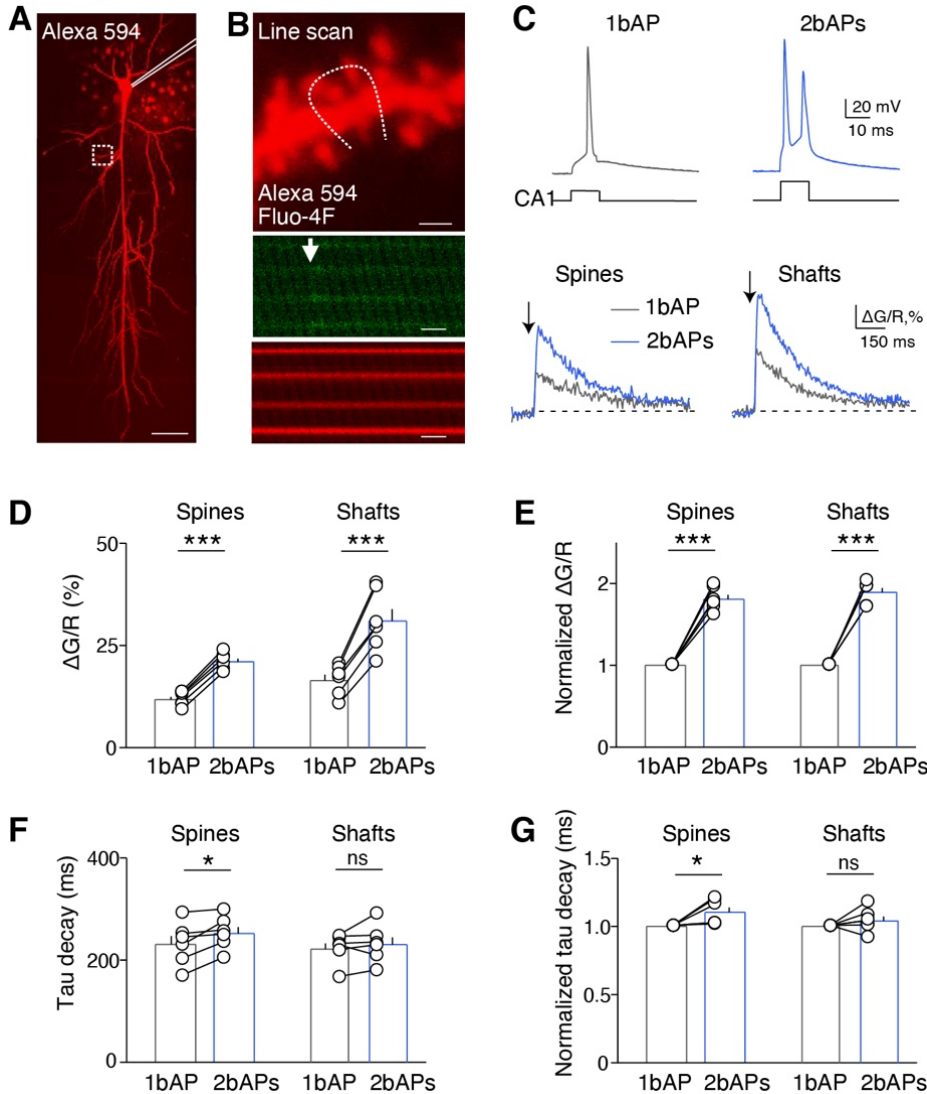
Fig. S6. Calcium transients in dendritic spines and shafts upon single or two bAPs.
(**A**) Combination of whole-cell recording of a CA1 pyramidal cell with two-photon imaging; the patch-clamp pipette is underlined in white and the dashed white square indicated the imaged dendritic area. The scanning areas had been selected on 50-150µm distance from soma. Scale bar: 30µm. (**B**) Line-scanning two-photon microscopy of Ca^{2+} transients in dendritic spines and adjacent shaft (top panel; scale bar: 2µm) filled with ratiometric indicators Fluo-4F (250µM; scale bar: 200ms) (middle panel) and Alexa Fluor 594 (50µM) (bottom panel; scale bar: 200ms). (**C**) A single or two bAPs were triggered in the recorded CA1 pyramidal cell by a postsynaptic current depolarization of 10 ms duration, and calcium transients were recorded in the dendritic spines and neighboring shafts. (**D** and **E**) Two bAPs induced larger increase of calcium in spines and shafts than a single bAP when evaluating ΔG/R (**D**) or the normalized ΔG/R (**E**). (**F** and **G**) Two bAPs induced a longer decay of the calcium transient in spines but not in shafts when compared to a single bAP, as estimated by the tau decay (**F**) and the normalized tau decay (**G**). Error bars represent the SEM. *: $p<0.05$; ***: $p<0.001$; ns: not significant.

13
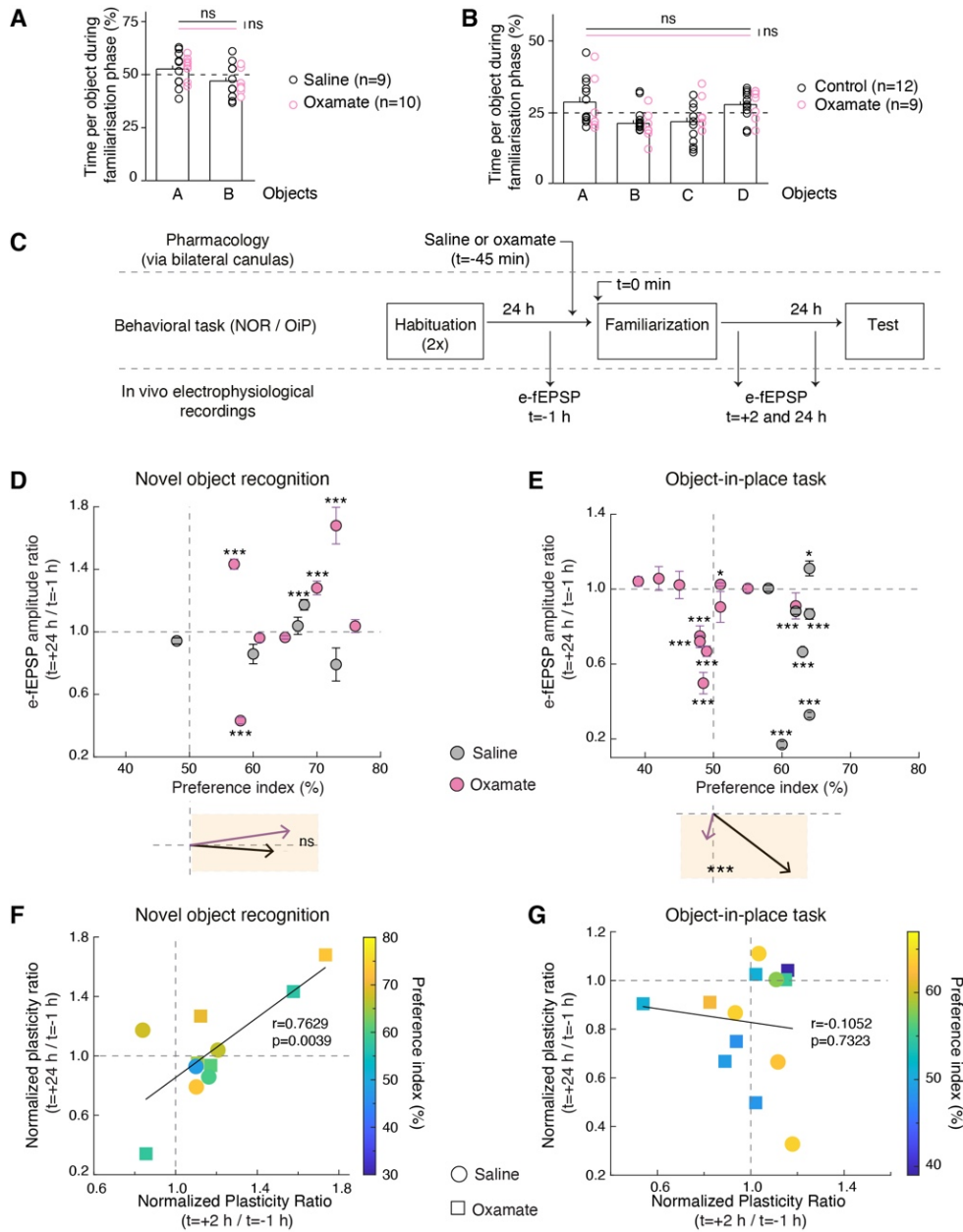
Fig. S7. *In vivo* synaptic plasticity 24 hours after test for NOR and OiP tasks (related to Figure 4).
(**A**) Rats injected in CA1 with saline or oxamate solutions spent similar amount of time exploring A and B (saline: *p*=0.3750, oxamate: *p*=0.1661, saline *vs* oxamate: object A: *p*=0.5563, object B: *p*=0.5563, one-way ANOVA). (**B**) Saline- or oxamate-injected rats explored similarly A, B, C and D (saline: *p*=0.1342, oxamate: *p*=0.2178, saline vs oxamate: A: *p*=0.8826, B: *p*=0.1342, C: *p*=0.2566, D: *p*=0.6964, one-way ANOVA). A and B were common for both NOR and OiP tasks. (**C**) Behavioral experimental set-up for the NOR and OiP tasks and e-fEPSP recordings. (**D** and **E**) No difference for e-fEPSP amplitudes 24 hours after familiarization were observed between saline or oxamate-injected rats, with on average no plasticity for the NOR task (**D**) and a majority of LTD for the OiP task (**C**) (see average vectors in **D** and **E**). (**F** and **G**) Correlation between e-LFPs recorded 2 and 24 hours after familiarization in the NOR and OiP tasks, in relation with the preference index. NOR: significant positive correlation with the plasticity ratios decreasing from +2 to +24 hours, with larger LTPs remaining LTP at +24 hours, while smaller LTPs shifting into no plasticity or LTD (similar for both saline- and oxamate-injected rats). OiP: no correlation between plasticity at +2 and +24 hours with LTP at +2 hours turned either into no plasticity or LTD while the majority of LTD at +2 hours persisted in LTD at +24 hours. All data are presented as mean±SD. *: p<0.05; **: p<0.01; ***: p<0.001; by two tailed *t*-test.
See *SI Appendix* Tables S4C and S4D for detailed data and statistics.

Tables S1 (related to Figure 1):

Experimental conditions	5-TBS EPSC amplitude % of baseline (n)	t-test, p value	2-way ANOVA, p value	STDP (50 pairings @ 0.5 Hz) EPSC amplitude % of baseline (n)	t-test, p value	2-way ANOVA, p value
Control	152.4 ±13.8(14)	0.0056	<0.0001	138.3 ± 10.2 (8)	0.0070	<0.0001
i-MK801	89.7 ± 6.4 (7)	0.1562	0.0801	103.4 ± 7.0 (7)	0.6484	0.4800
DAB	89.6 ± 10.5 (6)	0.3691	0.0651	91.8 ± 9.5 (7)	0.4213	0.0838
DAB + e-lactate[1] [2]	142.6 ± 17.0(6)	0.0311	0.0032	159.3 ± 24.1(7)	0.0383	0.0002
i-oxamate	91.7 ± 9.9 (9)	0.4600	0.0643	134.8 ± 14.0 (7)	0.0398	0.0008
i-oxamate + i-pyruvate	104.4 ± 13.3 (7)	0.7548	0.5110	-	-	-
i-oxamate + i-NADH[3]	158.5 ± 16.0 (6)	0.0145	<0.0001	-	-	-

[1], [2] and [3]: rescue experiments *vs* corresponding control (t-test, *p* value)
[1] 5-TBS: control *vs* e-DAB + e-lactate, *p*=0.6735
[2] STDP (1 Hz, 50 pairings): control *vs* e-DAB + e-lactate, *p*=0.4155
[3] 5-TBS: control *vs* i-oxamate + i-NADH, *p*=0.7995

Table S2. Parameter values of the mathematical model

Parameters	Description	Value	Unit
Parameters estimated from our experimental data			
g_L	Postsynaptic leak conductance	0.50	mS/cm^2
τ_{step}	Postsynaptic depolarization current time constant	15	ms
AT	Attenuation factor at the synapse	0.34	-
DP_{max}	Amplitude of the postsynaptic depolarization	1.50 (STDP 1bAP) 2.85 (STDP 2bAP) 0 (TBS)	mA/cm^2
DP_{dur}	Duration of the postsynaptic depolarization	10 (STDP) 0 (TBS)	ms
AP_{amp}	Amplitude of the bAP at the soma	120 (STDP 1bAP) 114 (STDP 2bAP) 130 (TBS)	mV
δ_1	Delay between depolarization onset and first bAP	7 (STDP 1bAP) 5.5 (STDP 2bAP)	ms
δ_2	Delay between first and second bAP	6.3 (STDP 2 bAP)	ms
α	Additional attenuation of the second bAP	0.65 (STDP 2 bAP)	-
τ_{Ca}	Time scale of cytosolic Ca dynamics	40	ms
τ_ρ	Time scale of the internal state variable	103.15	s
ρ^*	Unstable middle point of the bistable	0.257	-
LTD_{max}	Maximal amplitude of the LTD	70	-
LTD_{start}	Ca-threshold for the LTD	0.45	µM
LTP_{max}	Maximal amplitude of the LTP	120	-
LTP_{start}	Ca-threshold for the LTP	0.74	µM
M_{max}	Max. amplitude of the ATP-gated depotentiation	30	-
ATP_{Thr}	ATP-threshold of the ATP-gated depotentiation	1.87	mM
β_ρ	Final synaptic weight increase in LTP	0.405 (STDP 1baP) 0.405 (STDP 2baP) 0.550 (TBS)	-
τ_{AMPA1}	AMPA conductance time constant 1	9.6	ms
τ_{AMPA2}	AMPA conductance time constant 2	7.0	ms
$g_{AMPAmax}$	Max. AMPA conductance density	0.13	mS/cm^2
τ_{NMDA1}	NMDA conductance time constant 1	60.0	ms
τ_{NMDA2}	NMDA conductance time constant 2	1.0	ms
$g_{NMDAmax}$	Maximal NMDA conductance density	4.64×10^{-4}	mS/cm^2
g_{CaLmax}	Maximal CaL conductance density	0.0849	mS/cm^2
g_{Namax}	Maximal conductance density of VGSCs	11.5	mS/cm^2
Fixed parameters and constants			
$[Mg^{2+}]$	Magnesium concentration	1.0	mM
GLC_c	Glucose concentration in the bath solution in control	5.0	mM
E_{Ca}	Nernst Potential for Ca^{2+}	54[1]	mV
E_{NMDA}	Reversal potential NMDA receptors	0	mV
E_L	Reversal potential leak current	-70	mV
R	Gas constant	8.3145	J/mol/K
T	Temperature	310	K
F	Faraday Constant	96 485.3	C/mol
Fixed parameters taken from (*19*) with no change[2]			
$S_m v_x$	Surface/vol. ratio of compartment $x = \{a, n\}$	2.5×10^4	cm^{-1}
E_{AMPA}	Reversal potential AMPA receptors	0	mV
C_m	Membrane Capacitance postsynaptic compartment	10^{-3}	mF/cm^2
Na_e	Sodium extracellular concentration	150	mM
g_{Nax}	Na leak conductance in the postsynaptic compartment	0.0136 (*n*) 0.0061 (*a*)	mS/cm^2
V_a	Membrane voltage of the astrocyte	-70	mV
k_{pumpx}	Max. rate Na-K-ATPases	2.2×10^{-6} (*n*) 4.5×10^{-7} (*a*)	cm/mM/s

K_{Mpump}	Affinity constant for ATP of Na-K-ATPases	0.5	mM
K_{tg}	Affinity constant of glucose transporters	8	mM
Tg_{xy}	Constant of glucose transport between compartments x and y	0.0016 (*ca*) 0.0410 (*en*) 0.1470 (*ea*) 0.2390 (*ce*)	mM/s
k_{HKPFKx}	Maximal rate combined HK-PFK	0.0504 (*n*) 0.185 (*a*)	s^{-1}
K_g	Affinity for glucose HKPFK	0.05	mM
k_{PGKx}	Maximal rate PGK	3.97 (*n*) 135.2 (*a*)	mM^{-1}s^{-1}
N	Sum of NADH plus NAD$^+$ concentrations in control	0.212	mM
A	Total adenine nucleotide concentration	4.0 (*n*) 2.212 (*a*)	mM
C	Creatine plus phosphocreatine concentration	10	mM
q_{AK}	Adenylate kinase equilibrium constant	0.92	mM
k_{PKx}	Max. rate pyruvate kinase	36.7 (*n*) 401.7 (*a*)	mM^{-1}s^{-1}
k_{LDHonx}	Forward rate constant of LDH	72.3 (*n*) 1.59 (*a*)	mM^{-1}s^{-1}
$k_{LDHoffx}$	Backward rate constant of LDH	0.720 (*n*) 0.071 (*a*)	mM^{-1}s^{-1}
LAC_c	Lactate concentration in the reservoir	0.55	mM
Tl_{xy}	Constant of lactate transport between compartments x and y	24.3 (*ne*) 106.1 (*ae*) 0.00243 (*ac*) 0.25 (*ec*)	mM/s
K_{tlxy}	Affinity constant of lactate transporters between x and y	0.74 (*ne*) 3.50 (*ae*) 1.00 (*ac*) 1.00 (*ec*)	mM
$v_{\text{mitoin}x}$	Maximal rate of the TCA cycle	0.1303 (*n*) 5.7 (*a*)	mM/s
K_{Mmito}	Affinity constant TCA cycle for pyruvate	0.04	mM
K_{MNADx}	Affinity constant TCA cycle for NAD	0.409 (*n*) 40.3 (*a*)	mM
$v_{\text{mitoout}x}$	Maximal rate of the electron transport chain (ETC)	0.164 (*n*) 0.064 (*a*)	mM/s
K_{O2mito}	Affinity constant of ETC for O$_2$	0.001	mM
K_{MADPx}	Affinity constant of ETC for ADP	3.410 (*n*) 0.483 (*a*)	µM
K_{MNADHx}	Affinity constant of ETC for NADH	44.4(*n*) 26.9 (*a*)	µM
T_{NADHx}	Maximal rate for NADH shuttling	10330 (*n*) 150 (*a*)	mM/s
M_{cytox}	Constant for shuttling from cytosol	4.9×10^{-8} (*n*) 2.5×10^{-4} (*a*)	-
M_{mitox}	Constant for shuttling from mitochondria	3.93×10^5 (*n*) 1.06×10^4 (*a*)	-
k_{CKonx}	Forward rate of creatine kinase	0.0433 (*n*) 0.00135 (*a*)	mM^{-1}s^{-1}
k_{CKoffx}	Backward rate of creatine kinase	2.8×10^{-4} (*n*) 10^{-5} (*a*)	mM^{-1}s^{-1}
0_{2_c}	O$_2$ concentration in the bath solution	7	mM
PS_{cap}/V_x	O$_2$ transport constant from the reservoir	1.66 (*n*) 0.87 (*a*)	s^{-1}
K_{O2}	O$_2$ exchange constant	0.0361	mM
$Hb.OP$	O$_2$ exchange constant	8.6	mM
n_h	O$_2$ exchange Hill number	2.73	-
v_x	Relative volumes	0.45 (*n*) 0.25 (*a*)	-

		0.20 (*e*)	
ξ	Relative mitochondria volume	0.07	-
$J_{ATPasesx}$	ATPase activity of non-Na-K-ATPases	0.1695 (*n*)	mM/s
		0.1404 (*a*)	
J_{pumpa0}	Basal Na-K-ATPase activity	0 (*n*)	mM/s
		0. 0687 (*a*)	

[1]: after compensation for the slight K^+ permeability of CaL channels, see[41].

[2]: *n* is for the postsynaptic neuronal compartment, *a* for the astrocytic one, *e* for the extracellular pericellular volume and *c* for constant reservoir concentrations.

Tables S3 (related to Figures 2 and 3, *SI Appendix* Figures S4 and S5):

Experimental conditions	5-TBS except for [2]			STDP (50 pairings @ 0.5 Hz) except for [1, 4 and 5]		
	EPSC amplitude % of baseline (n)	t-test, *p* value	2-way ANOVA, *p* value	EPSC amplitude % of baseline (n)	t-test, p value	2-way ANOVA, *p* value
Control, 25mM glucose	169.7 ± 25.7 (8)	0.0299	<0.0001	-	-	-
i-oxamate, 25mM glucose	202.8 ± 20.9 (6)	0.0044	<0.0001	-	-	-
i-Mannoheptulose	134.6 ± 16.8 (7)	0.0230	0.0013	176.7 ± 24.7 (7)	0.0210	<0.0001
Control[1]	-	-	-	151.1±16.8 (8)	0.0191	<0.0001
i-mannoheptulose[1]	-	-	-	176.3±29.9 (6)	0.0436	0.0003
i-Mannoheptulose + i-oxamate[1]	-	-	-	86.6±19.9 (6)	0.5297	0.2856
i-oxamate[1]	-	-	-	151.1±16.8 (8)	0.0191	<0.0001
Control[2]	209.9±33.9 (6)	0.0229	<0.0001	-	-	-
i-oxamate[2]	162.4±15.8 (6)	0.0109	<0.0001	-	-	-
i-oxamate[3]	-	-	-	80.8±9.4 (6)	0.0956	0.0005
i-oxamate+i-NADH[3]	-	-	-	119.4±4.7 (7)	0.0061	0.0004
i-oxamate[4]	-	-	-	228.0±38.8 (6)	0.0216	<0.0001
Control[5]	-	-	-	123.1±8.6 (7)	0.0369	0.0117
i-oxamate[5]	-	-	-	129.0±9.8 (6)	0.0309	<0.0001
Control [6]	-	-	-	97.7±31.5 (6)	0.9439	0.4643
i-oxamate [6]	-	-	-	88.3±21.1 (7)	0.5992	0.0001
Control (mice) [1]	131.9±11.0 (5)	0.0441	0.0002	141.1±14.7 (6)	0.0454	<0.0001
i-oxamate (mice) [1]	70.1±6.8 (5)	0.0121	<0.0001	125.8±3.4 (5)	0.0024	<0.0001

[1] STDP with 100 pairings at 1 Hz, with control *vs* i-oxamate: *p*=0.9836, control *vs* i-oxamate + i-lactate: *p*=0.7095, control *vs* i-oxamate: *p*=0.9837 and i-oxamate *vs* i-oxmate + i-lactate: *p*=0.5901 (t-test)
[2] 1-TBS
[3] STDP with 50 pairings (2bAPs) at 1 Hz
[4] STDP with 25 pairings (2Aps) at 1 Hz
[5] STDP with 25 pairings (2bAPs) at 0.5 Hz
[6] intracellular solution with 2 mM ATP and 5 mM phosphocreatine

Tables S4A-D (related to Figure 4 and SI Appendix Figure S7):

A-

NOR task	Saline-injected rats		Oxamate-injected rats		Saline vs. oxamate
	Time per object (N) vs (F) / Preference index (n)	t-test, *p* value	Time per object / Preference index (n)	t-test, *p* value	t-test, *p* value
All	(N) 66.6±3.1% (F) 33.4±3.1% / 66.6±3.1 (9)	0.0007	(N) 67.6±3.2% (F) 32.4±3.2% / 67.6±3.2 (10)	0.0003	0.8126
AA-AB	(N) 71.8±2.9% (F) 28.2±2.9% / 71.8±2.9 (4)	0.0051	(N) 73.0±4.4% (F) 27.0±4.4% / 73.0±4.5 (5)	0.0063	0.8309
BB-BA	(N) 62.4±4.4% (F) 47.6±4.4% / 62.4±4.4 (5)	0.0475	(N) 62.3±3.3% (F) 37.7±3.3% / 62.3±3.3 (5)	0.0213	0.9792
AA-AB [1]	(N) 63.4±4.3% (F) 36.6±4.3% / 63.4±4.3 (5)	0.0370	(N) 65.9±2.8% (F) 47.6±2.8% / 65.9±2.8 (7)	0.0013	0.7617

[1]: rats with chronic recording and stimulation electrodes (e-fEPSPs), with bilateral cannulas.

(N) and (F): novel and familiar, respectively, objects.

B-

OiP task	Saline-injected rats		Oxamate-injected rats		Saline vs. oxamate
	Time per object (N) vs (F) / Preference index (n)	t-test, *p* value	Time per object / Preference index (n)	t-test, *p* value	t-test, *p* value
All	(N) 63.7±2.3% (F) 36.3±2.3% / 63.7±2.3 (12)	<0.0001	(N) 46.4±3.0% (F) 53.7±3.0% / 46.4±3.0 (9)	0.2500	0.0002
AC	(N) 68.6±3.2% (F) 31.4±3.2% / 68.6±3.2 (6)	0.0020	(N) 53.0±4.7% (F) 46.9±4.7% / 53.0±4.7 (4)	0.5603	0.0209
BD	(N) 58.9±2.0% (F) 41.1±2.0% / 58.9±2.0 (6)	0.0068	(N) 41.0±1.3% (F) 59.0±1.3% / 41.0±1.3 (5)	0.0026	<0.0001
AC [1]	(N) 61.7±1.2% (F) 38.3±1.2% / 61.7±1.2 (9)	<0.0001	(N) 49.1±1.7% (F) 50.9±1.7% / 49.1±1.7 (12)	0.6239	<0.0001

[1]: rats with chronic recording and stimulation electrodes (e-fEPSPs), with bilateral cannulas.

(N) and (F): novel and familiar, respectively, objects.

C- Evoked-fEPSP plasticity at 2 and 24 hours after familiarization phase in saline- and oxamate-injected rats in NOR and OiP tasks.

e-fEPSP monitoring	Saline-injected rats		Oxamate-injected rats		Saline *vs.* oxamate
	t post-familiarization: +2 h (n) + 24 h (n)	t-test, *p* value	*t* post-familiarization: +2 h (n) + 24 h (n)	t-test, *p* value	t-test, *p* value
NOR task	108.2±6.4 (5)	0.2686	128.0±10.7 (7)	0.0395	0.1839
	96.1±6.7 (5)	0.5904	112.1±15.3 (7)	0.4570	0.4210
OiP task	114.9±5.6 (7)	0.0377	93.7±6.3 (9)	0.3447	0.0287
	71.8±15.7 (7)	0.0778	87.3±6.6 (12)	0.0471	0.2380

D- Comparison of average vectors in saline- and oxamate-injected rats (MANCOVA)

Average vectors in saline- and oxamate-injected rats (MANCOVA)	Univariate test on the e-fEPSP plasticity axis		Univariate test on the behavior axis		Multivariate Test	
	F	*p* value	F	*p* value	F	*p* value
NOR task +2h	2.038	0.184	0.260	0.621	0.980	0.412
+24h	0.704	0.421	0.260	0.621	0.353	0.712
OiP task +2h	5.94	0.029	16.43	0.01	14,7	<0.001
+24h	1.50	0.238	28.82	< 0.001	13.9	<0.001

SI References
1. Feldman, D. E. The spike-timing dependence of plasticity. Neuron 75, 556–571 (2012).
2. Xu, H. et al. Dopamine-endocannabinoid interactions mediate spike-timing-dependent potentiation in the striatum. Nat Commun 9, 1, 4118 (2018).
3. Graupner, M. & Brunel, N. Calcium-based plasticity model explains sensitivity of synaptic changes to spike pattern, rate, and dendritic location. Proc Natl Acad Sci U S A 109, 10, 3991-6 (2012).
4. R. Jolivet, J. S. Coggan, I. Allaman, P. J. Magistretti, Multi-timescale modeling of activity-dependent metabolic coupling in the neuron-glia-vasculature ensemble. PLoS Comput Biol 11, 2, e1004036 (2015).
5. Roberts, P. AMPA Glutamate Receptor (AMPA Receptor), Conductance Models. In Jaeger D., Jung R. (eds) *Ency Comput Neurosci* 2014 Springer, New York, NY (2014).
6. Roberts, P. N-Methyl-D-Aspartate (NMDA) Receptors, Conductance Models. In: Jaeger D., Jung R. (eds) *Ency Comput Neurosci*, 2014 Springer, New York, NY (2014).
7. Solinas, S., Masoli, S. & Subramaniyam, S. High-Voltage-Activated Calcium Channels. In Jaeger D., Jung R. (eds) *Ency Comput Neurosci* 2014 Springer, New York, NY. (2014).
8. Migliore, M., Ferrante, M. & Ascoli, G. A. Signal propagation in oblique dendrites of CA1 pyramidal cells. *J Neurophysiol* 94, 6, 4145-55 (2005).
9. Watanabe, S., Hoffman, D. A., Migliore, M. & Johnston, D. Dendritic K+ channels contribute to spike-timing dependent long-term potentiation in hippocampal pyramidal neurons. Proc Natl Acad Sci U S A 99, 12, 8366-71 (2002).
10. Sabatini, B. L., Oertner, T. G. & Svoboda, K. The life cycle of Ca(2+) ions in dendritic spines. *Neuron* 33, 3, 439-52 (2002).
11. Carter, A. G. & Sabatini, B. L. State-dependent calcium signaling in dendritic spines of striatal medium spiny neurons. *Neuron* 44, 3, 483-93 (2004).
12. K. A. Kasischke, H. D. Vishwasrao, P. J. Fisher, W. R. Zipfel, W. W. Webb, Neural activity triggers neuronal oxidative metabolism followed by astrocytic glycolysis. *Science* 305, 5680, 99-103 (2004).